Continuum Mech. Thermodyn. (2025) 37:63
https://doi.org/10.1007/s00161-025-01397-6

ORIGINAL ARTICLE

Koffi Enakoutsa · Ivan Giorgio

Advanced constitutive modeling of flexoelectric materials incorporating higher-order gradient effects: Towards the design and optimization of nanoscale devices

Received: 16 February 2025 / Accepted: 29 May 2025 / Published online: 7 June 2025
© The Author(s), under exclusive licence to Springer-Verlag GmbH Germany, part of Springer Nature 2025

Abstract This work presents a comprehensive theoretical framework for flexoelectric materials by incorporating higher-order strain gradient and polarization gradient effects into the constitutive modeling. Using an extended strain gradient elasticity (SGE) approach, coupled with a generalized Toupin-like variational formulation, we derive governing equations, balance laws, and boundary conditions based on an enriched internal energy density function. Analytical solutions, expressed in terms of modified Bessel functions, provide key insights into the role of higher-order gradients in influencing displacement, polarization, and electric fields. The study highlights the critical impact of size effects on flexoelectric response, revealing that reducing material thickness enhances sensitivity and energy conversion efficiency. Furthermore, numerical simulations validate the theoretical model and demonstrate its applicability in the design of nanoscale flexoelectric sensors and energy harvesters. These findings establish a robust theoretical foundation for optimizing nanoscale electromechanical devices, with potential applications in biomedical sensors, structural health monitoring, and energy-efficient electronics.

Keywords Flexoelectric materials · Polarization · Constitutive models · Analytical Solution · Optimization

Contents

1 Introduction . . . 2
2 Governing equations . . . 3
2.1 Centrosymmetric materials . . . 5
3 Case study: Polarization in a thick-walled cylindrical tube . . . 6
3.1 Outline of the approach . . . 7
4 Illustration of the flexoelectric response . . . 11
4.1 Implementation . . . 12
4.2 Results and discussion . . . 12

I. Giorgio contributed equally to this work.

K. Enakoutsa
Department of Mathematics, University of California Los Angeles, 520 Portola Plaza, Los Angeles 951555, CA, USA
E-mail: koffi@math.ucla.edu

K. Enakoutsa · I. Giorgio (✉)
International Research Center for the Mathematics and Mechanics of Complex Systems (M&MoCS), University of L'Aquila, L'Aquila 67100, Italy
E-mail: ivan.giorgio@univaq.it

I. Giorgio
Department of Civil, Construction-Architectural and Environmental Engineering (DICEAA), University of L'Aquila, L'Aquila 67100, Italy

4.2.1 Mathematical perspective . . . 12
4.2.2 Physical perspective . . . 12
4.2.3 Mechanics Perspective . . . 13
4.2.4 Boundary Conditions Validation . . . 13
4.3 Analysis of the results with flexoelectric effects . . . 14
5 Size effects analysis of the analytic solution . . . 17
5.1 Analytical solutions . . . 18
5.2 Boundary conditions and coefficient dependencies . . . 18
5.3 Asymptotic behavior . . . 18
6 Dimensionless parameters and size effects . . . 19
Definition of dimensionless parameters . . . 19
Dimensionless form of analytical solutions . . . 19
Scaling relationships . . . 20
Size effects in the analytical solutions . . . 20
Impact of dimensionless parameters on device performance . . . 20
7 Energy harvesting and sensing implications . . . 20
7.1 Energy harvesting applications . . . 20
7.1.1 Cantilever-based energy harvester . . . 21
7.1.2 Thin film devices . . . 22
7.1.3 Multi-layered structures . . . 26
7.1.4 Energy harvesting efficiency application . . . 27
7.2 Sensing applications . . . 28
7.2.1 Pressure sensor for biomedical monitoring . . . 29
7.2.2 Tactile detection in soft robotics . . . 32
7.2.3 Ultrasonic pressure sensing . . . 35
8 Concluding remarks . . . 38
A Approximate solutions for the polarization field . . . 40
A.1 Displacement and strain expressions . . . 40
A.2 Asymptotic approximations of bessel functions . . . 40
A.3 Approximating the polarization field . . . 41
A.4 Discussion and physical implications . . . 41
References . . . 41

1 Introduction

Scientific research often progresses through a balance between theoretical development and practical applications. Flexoelectricity, a phenomenon that coupling mechanical strain gradients with electric polarization, represents a frontier where fundamental physics meets the demands of modern nanotechnology. At the macroscale, flexoelectric effects are often negligible due to relatively small strain gradients; see the pioneering works of [38,40,54] and later of [60,61]. However, as material dimensions shrink to the micro or nanoscale, these effects become pronounced, as demonstrated in recent studies by [55] and [18,62–65], opening pathways for innovative applications in diverse fields. This shift underscores the need for advanced theoretical frameworks to understand and exploit flexoelectricity in nanoscale devices such as energy harvesters, sensors, transducers, and resonators.

Flexoelectricity is especially relevant in the design of devices that require precise electromechanical interactions. In the biomedical field, flexoelectric materials have shown promise in the creation of sensors capable of detecting minute biomechanical forces, such as those generated by cardiac or neural activity. These sensors, integrated with wearable or implantable devices, can provide real-time monitoring and diagnostics, transforming patient care. In addition, flexoelectric nanostructures have found utility in environmental monitoring, enabling the development of ultrasensitive pressure or acoustic sensors to detect changes in atmospheric conditions or underwater ecosystems.

Another emerging application lies in energy harvesting, where flexoelectric materials convert mechanical vibrations into electrical energy. This capability is particularly valuable for powering nanoscale devices, such as wireless sensors or microelectromechanical systems (MEMS), in remote or hard-to-access environments. For example, flexoelectric nanowires embedded in the wings of drones or on bridges can harness ambient vibrations to generate power, reducing the reliance on external energy sources.

Theoretical modeling of flexoelectricity has evolved significantly, drawing from both classical elasticity theories (e.g., [36,45–47,67]) and modern strain gradient formulations (e.g., [13–17,66]). However, many existing models, being limited to first-order gradients [30,32,33,49,56] fail to capture higher-order effects, which are critical to accurately predicting the behavior of nanoscale systems. The limited presence of a comprehensive theoretical framework in the literature highlights the need for a more robust framework that

combines second-order gradient and polarization gradient theories, or possibly even higher-order theories [1–6], to better understand size-dependent phenomena. These approaches, supported by experimental validation ([7,8,42–44,56,68,69]), provide a foundation for studying size-dependent electromechanical behavior.

This work presents an enhanced theoretical framework that incorporates strain gradient elasticity (SGE) to incorporate higher-order effects. It is coupled with a Toupin-like variational formulation [13–16,20] by extending the internal energy density function to include second-order strain gradients and polarization gradients. By applying this framework to the analysis of thick-walled cylindrical tubes under axisymmetric loading, we derive analytical solutions that reveal the critical role of higher-order gradients in influencing mechanical and electromechanical responses. Beyond theoretical development, the framework demonstrates practical utility in optimizing the performance of nanoscale sensors and energy harvesters, addressing the pressing need for efficient, reliable, and scalable solutions in advanced electronics, biomedical devices, and environmental technologies. Moreover, utilizing a variational formulation enables the straightforward unification of various physical characteristics, such as mechanical properties, flexoelectricity, piezoelectricity, and damage accumulation [21–23], among others. Furthermore, this formulation provides us with a tool that can be directly employed in FEM simulations (see, e.g., [24–26] for high-order gradient applications).

In addition to theoretical development, this work bridges the gap to practical applications by demonstrating how the extended model informs design optimization for energy harvesting and sensing devices. By explicitly considering the interaction between higher-order gradients and flexoelectric couplings, the model guides the selection of material parameters and geometric configurations for performance enhancement. To illustrate the capabilities of the model, the paper explores its application to a thick-walled cylindrical tube subjected to axisymmetric loading. Analytical solutions expressed in terms of modified Bessel functions reveal the significant impact of higher-order gradients, offering insights into stress and polarization fields near defects.

In the following sections, we delve into the derivation of governing equations, balance laws, and boundary conditions, showcasing the interplay between higher-order gradients and flexoelectric coupling. We further explore the application of the model to optimize device performance, emphasizing its potential to transform the design and functionality of nanoscale electromechanical systems.

2 Governing equations

In this section, we present the constitutive equations relevant to elastic flexoelectric materials. Derived under the assumption of small deformations, these equations rely on an internal energy density $\mathcal{W}$ [28]. This potential energy extends the model proposed by [57] and utilized by [56], and is defined as follows:

$$\begin{aligned}\mathcal{W}\left(D_{ij}, D_{ij,k}, P_i, P_{i,j}\right) = &\frac{1}{2}C_{ijkl}D_{ij}D_{kl} + \frac{1}{2}H_{ijklmn}D_{ij,k}D_{lm,n} + \frac{1}{2}\chi_{ij}P_iP_j \\ &+e_{ijk}P_iD_{jk} + G_{ijklm}D_{ij}D_{kl,m} + K_{ijkl}P_iD_{jk,l} + a_{ij}P_{i,j} \\ &+\frac{1}{2}b_{ijkl}P_{i,j}P_{k,l} + d_{ijkl}P_{i,j}D_{kl} + g_{ijk}P_iP_{k,j} \end{aligned} \tag{1}$$

The energy density described by (1) is a quadratic form that involves two kinematical descriptors: the mechanical displacement $\boldsymbol{u} \equiv u_i \in \mathbb{R}^3$ and the polarization vector $\boldsymbol{\mathcal{P}} \equiv P_i \in R^3$, together with their spatial derivatives, which are denoted by the comma symbol. Herein, we utilize the Einstein convention in which repeated indices signify a sum. The measure of deformation $\boldsymbol{\mathcal{D}} \equiv D_{ij}$ is the classical second-rank symmetric strain tensor, which is defined as by:

$$D_{ij} = \frac{1}{2}\left(u_{i,j} + u_{j,i}\right)$$

The constitutive tensors appearing in Eq. (1) are: 1) the fourth-rank elastic stiffness tensor with zero polarization, $\boldsymbol{\mathcal{C}} \equiv C_{ijkl}$; 2) the third-rank piezoelectric tensor, $\boldsymbol{e} \equiv e_{ijk}$ [11,12]; 3) the sixth- and fifth-rank tensors, respectively, denoted by $\boldsymbol{\mathcal{H}} \equiv H_{ijklmn}$ and $\boldsymbol{\mathcal{G}} \equiv G_{ijklm}$ that represent the second-gradient elastic stiffness and the first/second-gradient coupling tensor with vanishing polarization, as suggested by [13–16]; 4) the fourth-rank flexoelectric tensor, $\boldsymbol{\mathcal{K}} \equiv K_{ijkl}$; 5) the classical second-order reciprocal dielectric susceptibility tensor with zero strain, $\boldsymbol{\chi} \equiv \chi_{ij}$; 6) the fourth-order tensor which connects the gradient of polarization to the strain $\boldsymbol{d} \equiv d_{ijkl}$ [47]; 7) the polarization gradient-polarization gradient coupling fourth-order tensor, $\boldsymbol{b} \equiv b_{ijkl}$; 8) the material tensor that links the polarization with the gradient of the polarization, $\boldsymbol{g} \equiv g_{ijk}$, as introduced by

[47]; 9) the material tensor linked to the gradient of the polarization at zero strain, $\boldsymbol{a} \equiv a_{ij}$, introduced to avoid strain and polarization localization at the surface of the body, see [47].

The elastic stiffness tensor $\mathcal{C}$ together with the SGE tensors $\mathcal{H}$ and $\mathcal{G}$ in Eq. (1) satisfy these symmetry properties:

$$\begin{cases} C_{ijkl} &= C_{klij} \\ H_{ijklp} &= H_{lpijkl} \\ G_{ijklpq} &= G_{lpqijk} \end{cases} \tag{2}$$

The symmetry properties of the strain tensor $\mathcal{D}$ impose these further symmetries on the tensors $\mathcal{C}$, $\mathcal{H}$, and $\mathcal{G}$:

$$\begin{cases} C_{ijkl} &= C_{ijlk} = C_{jikl} \\ H_{ijklp} &= H_{jiklp} = H_{ijkpl} \\ G_{ijklpq} &= G_{jiklpq} = G_{ijkplq} \end{cases} \tag{3}$$

To finalize the discussion on the symmetry of the material tensors defining the internal energy density (1), it is worth noting that the details of the symmetry for the tensors $\boldsymbol{b}$ and $\boldsymbol{d}$ are available in [48]. For insights on the flexoelectric tensor $\mathcal{K}$, references [37,38] can be consulted. The recent research conducted by [39] also offers an in-depth analysis of the mathematical characteristics of the flexoelectric tensor. The piezoelectric tensor $\boldsymbol{e}$ obeys the conventional symmetry properties described as follows:

$$e_{ijk} = e_{jik}$$

The energy expression described in (1) builds upon the model introduced by [49], incorporating further effects of strain-gradient elasticity and coupling terms for both polarization and its gradient. The function representing the internal energy density also incorporates piezoelectric coupling effects, similar to the approach presented in [49]. Our aim is to encompass a broad range of materials in our analysis, including both centrosymmetric and non-centrosymmetric types, as well as piezoelectrics and non-piezoelectrics. We remark that for centrosymmetric materials, all odd-order rank material tensors disappear (see, e.g., [47] and [13]), thus allowing recovery of the internal energy density function proposed by [56].

The internal energy density given by (1) provides the basis for defining an internal energy functional denoted as $\mathcal{E}^i$ as follows:

$$\mathcal{E}^{\mathrm{i}} = \int_\Omega \mathcal{W}\,\mathrm{d}V = \frac{1}{2}\int_\Omega \left(\Sigma_{ij}D_{ij} + M_{ijk}D_{ij,k} - E_i P_i + E_{ij}P_{i,j}\right)\,\mathrm{d}V \tag{4}$$

where the new terms appearing in Eq. (4) include the Cauchy stress Σ_{ij}, the hyperstress M_{ijk}, the local electric force E_i, the higher-order local electric force E_{ij}, and the strain gradient $D_{ij,k}$ and are specified as:

$$\begin{cases} \Sigma_{ij} &= \dfrac{\partial \mathcal{W}}{\partial D_{ij}} = C_{ijkl}D_{kl} + G_{ijklm}D_{kl,m} + e_{ijk}P_k \\ M_{ijk} &= \dfrac{\partial \mathcal{W}}{\partial D_{ij,k}} = G_{ijklp}D_{lp} + H_{ijklpq}D_{lp,q} + K_{ijkl}P_l \\ E_i &= -\dfrac{\partial \mathcal{W}}{\partial P_i} = e_{ijk}D_{jk} + K_{ijkl}D_{jk,l} + \chi_{ij}P_j \\ E_{ij} &= \dfrac{\partial \mathcal{W}}{\partial P_{i,j}} = b_{ijkl}P_{k,l} + d_{ijkl}D_{kl} + g_{ijk}P_k + a_{ij} \end{cases} \tag{5}$$

The work of the external forces $\mathcal{E}^{\mathrm{e}}$ is defined as follows:

$$\mathcal{E}^{\mathrm{e}} = \int_\Omega \left(f_i u_i + E_i^0 P_i\right)\,\mathrm{d}V + \int_{\partial\Omega} \left(t_i u_i + h_i Du_i\right)\,\mathrm{d}A \tag{6}$$

where f_i is the external body force per unit volume, E_i^0 denotes the external electric field, t_i is the traction vector on the boundary, h_i is the double stress traction vector, $Du_i = n_l u_{i,l}$ is the normal (directional) derivative

of the displacement component u_i, being n_l the normal unit vector outward to the surface $\partial\Omega$, which is the closed smooth boundary surface of Ω where external interactions are applied. For the sake of simplicity, in Eq. (6), we omit the boundary conditions of the electric nature in terms of the polarization vector $\mathcal{P}$ and the local higher order electric force E_{ij}.

Variational methods such as those presented in [34,47,67] will be employed to derive the balance equations along with the boundary conditions. To achieve this, an extra component must be incorporated into the integrand (i.e., the energy density function) of the energy density (1) to align with the variational methods described in [67] and [47]. Consequently, the revised energy density function is represented as:

$$\tilde{\mathcal{W}} = \frac{1}{2}\left(\Sigma_{ij} D_{ij} + M_{ijk} D_{ij,k} - E_i P_i + E_{ij} P_{i,j}\right) - \frac{1}{2}\epsilon_0 \left(\nabla\Phi\right)_i \left(\nabla\Phi\right)_i + \left(\nabla\Phi\right)_i P_i \tag{7}$$

where Φ denotes an electric potential that is associated with the local electric force E_i in the following manner:

$$E_i = \left(\nabla\Phi\right)_i = \Phi_{,i} \tag{8}$$

Using this revised expression for the density function, the variational methods from [34,47,67] can be employed on the internal energy (7) and the external energy (6) for a body occupying the volume Ω, which is enclosed by the boundary $\partial\Omega$, which separates Ω from the external vacuum $\Omega^\star$. This leads to the derivation of the following balance equations within the framework of quasi-static analysis:

$$\begin{cases} \Sigma_{ij,j} - M_{ijk,jk} + f_i = 0 \\ E_i + E_{ij,j} - \left(\nabla\Phi\right)_i + E_i^0 = 0 \\ -\epsilon_0 \left(\nabla\Phi\right)_{ii} + P_{i,i} = 0 \quad \text{in} \quad \Omega \\ \left(\nabla\Phi\right)_{ii} = 0 \quad \text{in} \quad \Omega^\star \end{cases} \tag{9}$$

along with the boundary conditions:

$$\begin{cases} \Sigma_{ij} n_j - \left(M_{ijk} n_k\right)_{,j} + \left(M_{ijk} n_k n_j\right)_{,l} n_l = t_i \\ M_{ijk} n_j n_k = h_i \\ n_i \left(-\epsilon_0 \left[\left[\left(\nabla\Phi\right)_i\right]\right] + P_i\right) = 0 \\ n_i E_{ij} = 0 \end{cases} \tag{10}$$

where the notation $\left[\left[\left(\nabla\Phi\right)_i\right]\right]$ represents the jump in $\left(\nabla\Phi\right)_i$ across the bounding surface $\partial\Omega$.

Equations (9), combined with the boundary conditions (10) and the constitutive relations (5), form the generalized governing framework for elastic flexoelectric materials when subjected to small deformations.

2.1 Centrosymmetric materials

In centrosymmetric materials, the piezoelectric coefficient tensor $\boldsymbol{e}$, the Mindlin tensor $\boldsymbol{g}$ that associates polarization with its gradient, and the fifth rank elastic strain gradient tensor $\mathcal{G}$ are all zero [47]. Thus, the constitutive relationships (5) simplify to:

$$\begin{cases} \Sigma_{ij} &= C_{ijkl} D_{kl} \\ M_{ijk} &= H_{ijklpq} D_{lp,q} + K_{ijkl} P_l \\ E_i &= K_{ijkl} D_{jk,l} + \chi_{ij} P_j \\ E_{ij} &= b_{ijkl} P_{k,l} + d_{ijkl} D_{kl} + a_{ij} \end{cases} \tag{11}$$

For isotropic elastic materials exhibiting homogeneous flexoelectric properties, the elastic stiffness tensor $\mathcal{C}$ simplifies to the standard Lamé constants λ and μ. As demonstrated by [13], who initially used the material symmetry principles from [58], the tensors $\mathcal{H}$ and $\mathcal{G}$ simplify to:

$$\mathcal{G}_{ijklp} = 0 \tag{12}$$

and

$$\begin{cases} H_{ijklpq} = c_1\left(\delta_{ij}\delta_{kl}\delta_{pq} + \delta_{ij}\delta_{kp}\delta_{lq} + \delta_{ik}\delta_{jq}\delta_{lp} + \delta_{iq}\delta_{jk}\delta_{lp}\right) \\ \qquad\quad +c_3\left(\delta_{ik}\delta_{jl}\delta_{pq} + \delta_{ik}\delta_{jp}\delta_{lq} + \delta_{il}\delta_{jk}\delta_{pq} + \delta_{ip}\delta_{jk}\delta_{lq}\right) \\ \qquad\quad +c_5\left(\delta_{il}\delta_{jq}\delta_{kp} + \delta_{ip}\delta_{jq}\delta_{kl} + \delta_{iq}\delta_{jl}\delta_{kp} + \delta_{iq}\delta_{jp}\delta_{kl}\right) \\ \qquad\quad +c_2\delta_{ij}\delta_{kq}\delta_{lp} + c_4(\delta_{il}\delta_{jp}\delta_{kq} + \delta_{ip}\delta_{jl}\delta_{kq}) \end{cases} \tag{13}$$

where δ_{ij} represents the Kronecker delta tensor, and c_i indicates the elastic material constants associated with strain gradients, specific to various materials.

Furthermore, Masson [41], Mindlin [47], and Maranganti and coworkers [52] demonstrated that for linear isotropic centrosymmetric materials, the tensors $\mathcal{K}$, $\boldsymbol{\chi}$, $\boldsymbol{a}$, $\boldsymbol{d}$, and $\boldsymbol{b}$ can be reduced in terms of their components to:

$$\begin{cases} K_{ijkl} = k_{12}\delta_{ij}\delta_{kl} + k_{44}\left(\delta_{ik}\delta_{jl} + \delta_{il}\delta_{jk}\right) \\ \chi_{ij} = \chi\delta_{ij}. \\ a_{ij} = a\delta_{ij} \\ d_{ijkl} = d_{12}\delta_{ij}\delta_{kl} + d_{44}\left(\delta_{ik}\delta_{jl} + \delta_{il}\delta_{jk}\right) \\ b_{ijkl} = b_{12}\delta_{ij}\delta_{kl} + b_{44}\left(\delta_{ik}\delta_{jl} + \delta_{il}\delta_{jk}\right) + b_{77}\left(\delta_{ik}\delta_{jl} - \delta_{il}\delta_{jk}\right) \end{cases} \tag{14}$$

Consequently, we derive the following electromechanical stresses from Eqs. (11), (12), (13), and (14):

$$\begin{cases} \Sigma_{ij} = \lambda D_{kk}\delta_{ij} + 2\mu D_{ij} \\ M_{ijk} = 2c_1 D_{kp,p}\delta_{ij} + c_1 D_{pp,j}\delta_{ik} + c_1 D_{pp,i}\delta_{jk} + c_2 D_{ll,k}\delta_{ij} \\ \qquad\quad +2c_3(D_{jq,q}\delta_{ik} + D_{iq,q}\delta_{jk}) + 2c_4 D_{ij,k} + 2c_5(D_{ik,j} + D_{jk,i}) \\ \qquad\quad +\delta_{ij}k_{12}P_k + k_{44}\left(\delta_{ik}P_j + \delta_{jk}P_i\right) \\ E_i = k_{12}D_{ik,k} + k_{44}\left(D_{ji,j} + D_{jj,i}\right) + \chi P_i \\ E_{ij} = b_{12}\delta_{ij}P_{k,k} + b_{44}(P_{j,i} + P_{i,j}) + b_{77}(P_{j,i} - P_{i,j}) \\ \qquad\quad +d_{12}\delta_{ij}D_{kk} + 2d_{44}D_{ij} + a\delta_{ij} \end{cases} \tag{15}$$

The constitutive equation (15) incorporates fourteen constitutive parameters, alongside the two conventional Lamé elasticity coefficients, all of which are dependent on the kind of material. In what follows, we will demonstrate the capabilities of the newly introduced model through the resolution of the polarization problem of a thick-walled cylindrical tube under axisymmetric loading conditions.

3 Case study: Polarization in a thick-walled cylindrical tube

This study focuses on a cylindrical tube with thick walls, where the inner and outer radii are denoted as r_i and r_e, respectively. The cylindrical matrix follows the constitutive equation (15) and is subjected to axisymmetric load conditions. The problem under study, addressed within the framework of linearized theory, where strain and displacement remain small, is depicted in Figs. 1 and 2. The classical cylindrical coordinates r, θ and z and the corresponding orthogonal basis $\mathbf{e}_r$, $\mathbf{e}_\theta$, $\mathbf{e}_z$ are used. Under the assumption of plane strain conditions, the displacement component in the z-direction is zero. We investigate an axisymmetric problem where the displacement field $\mathbf{U}$, the polarization field $\mathbf{P}$, and the electric potential Φ are regarded as radial. Specifically, we express $\mathbf{U} \equiv U(r)\mathbf{e}_r$, $\mathbf{P} \equiv P(r)\mathbf{e}_r$, and $\Phi \equiv \Phi(r)$.

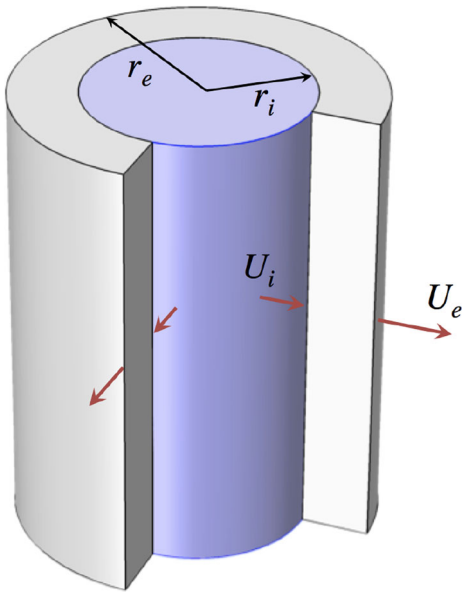


Fig. 1 Polarization in a thick-walled cylindrical tube under axisymmetric loading conditions. The cylindrical tube has inner and outer radii denoted as r_i and r_e, respectively, utilizing the curvilinear cylindrical coordinate system $\mathbf{e}_r$, $\mathbf{e}_\theta$, $\mathbf{e}_z$

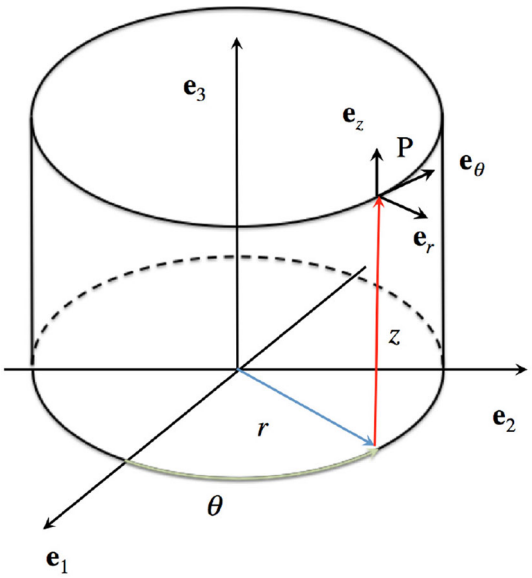


Fig. 2 Scheme of classical cylindrical coordinates r, θ, and z, alongside the associated orthogonal basis vectors $\mathbf{e}_r$, $\mathbf{e}_\theta$, and $\mathbf{e}_z$

In the course of addressing this problem, we employ the subsequent mathematical property concerning radial vectors: for a specific conservative vector field $\mathbf{W}$, which can be expressed by the gradient of a potential function, the equation $\Delta\mathbf{W} = \nabla(\mathrm{div}\,\mathbf{W})$, which means in components:

$$W_{i,hh} = W_{h,hi} \tag{16}$$

is valid. The demonstration of this property is straightforward and is available in [19].

3.1 Outline of the approach

We assume throughout the following discussion that $\mathbf{W} = \Delta\mathbf{U}$. From this assumption, we derive:

$$D_{hh,i} = \mathrm{U}_{h,hi} = W_i \quad \text{and} \quad D_{ih,h} = \frac{1}{2}(U_{i,hh} + U_{h,ih}) = U_{i,hh} = \Delta U_i \tag{17}$$

and

$$D_{hh,i} = D_{ih,h} = W_i \tag{18}$$

The solution process begins by calculating the first spatial derivatives of both the stress and the higher order electric force, alongside the second spatial derivatives of the hyperstress, as per Eq. $(15)_{1,2}$; resulting in

$$\begin{cases} \Sigma_{ij,j} &= \lambda D_{kk,i} + 2\mu D_{ij,j} \\ M_{ijk,jk} &= c_1\left(2D_{kp,pik} + D_{pp,jji} + D_{pp,ikk}\right) + c_2 D_{ll,kik} \\ &\quad +2c_3(D_{jq,qji} + D_{iq,qjk}) + 2c_4 D_{ij,kjk} \\ &\quad +2c_5(D_{ik,jjk} + D_{jk,ijk}) + (k_{12} + k_{44})\, P_{k,ik} + k_{44} P_{i,jj}. \\ E_{ij,j} &= b_{12} P_{k,ki} + b_{44}(P_{j,ij} + P_{i,jj}) + b_{77}(P_{j,ij} - P_{i,jj}) \\ &\quad +d_{12} D_{kk,i} + 2d_{44} D_{ij,j} \end{cases} \tag{19}$$

Using the properties (18), equations (19) and $(15)_3$ transform into

$$\begin{cases} \Sigma_{ij,j} &= (\lambda + 2\mu)\, W_i \\ M_{ijk,jk} &= (4c_1 + c_2 + 4c_3 + 2c_4 + 4c_5)(\Delta W)_i \\ &\quad + (k_{12} + k_{44})\, P_{k,ik} + k_{44}(\Delta P)_i \\ E_i &= (k_{12} + 2k_{44})\, W_i + a P_i \\ E_{ij,j} &= (d_{12} + 2d_{44} + b_{12} + 2b_{44})\, W_i \end{cases} \tag{20}$$

We now consider incorporating the spatial derivatives of both the stress and hyperstress tensors, referenced in $(20)_{1,2}$, along with the electric field $(20)_3$ and its derivative $(20)_4$, into the balance equations (15); this yields

$$\begin{cases} W_i - \dfrac{(4c_1 + c_2 + 4c_3 + 2c_4 + 4c_5)}{\lambda + 2\mu}(\Delta W)_i \\ \qquad + \dfrac{k_{12} + k_{44}}{\lambda + 2\mu} P_{k,ik} + \dfrac{k_{44}}{\lambda + 2\mu}(\Delta P)_i + \dfrac{1}{\lambda + 2\mu} f_i = 0 \\ (k_{12} + 2k_{44} + d_{12} + 2d_{44} + b_{12} + 2b_{44})\, W_i + a P_i - (\nabla \Phi)_i + E_i^0 = 0 \end{cases} \tag{21}$$

It is clear in Eq. (21) that the displacement and polarization fields are coupled by the flexoelectric constants K_{ijkl}. When there are no external mechanical or electrical forces acting on the body, i.e., $f_i = E_i^0 = 0$, the differential equations system (21) simplifies to

$$\begin{cases} W_i - k^1(\Delta W)_i + k^2 P_{k,ik} + k^3(\Delta P)_i = 0 \\ k^4 W_i - (\nabla \Phi)_i + \chi P_i = 0 \end{cases} \tag{22}$$

where

$$\begin{cases} k^1 = \dfrac{4c_1 + c_2 + 4c_3 + 2c_4 + 4c_5}{\lambda + 2\mu} \\ k^2 = \dfrac{k_{12} + k_{44}}{\lambda + 2\mu} \\ k^3 = \dfrac{k_{44}}{\lambda + 2\mu} \\ k^4 = k_{12} + d_{12} + b_{12} + 2\,(k_{44} + d_{44} + b_{44}) \end{cases} \tag{23}$$

Taking into account the third component of the balance equations (9), as referred to by $(9)_3$, the expressions (22) simplify to

$$\begin{cases} W_i - k^1(\Delta W)_i + k^2 P_{k,ik} + k^3(\Delta P)_i = 0 \\ k^4 W_{i,i} - \tilde{\chi}\, P_{i,i} = 0 \end{cases} \tag{24}$$

where $\tilde{\chi} = (\epsilon_0 \chi - 1)/\epsilon_0$. By substituting Eq. $(24)_2$ into Eq. $(22)_1$, we derive the following expression:

$$W_i - k^1(\Delta W)_i + k^2 P_{k,ik} - \frac{k^3 k^4}{\tilde{\chi}}(\Delta W)_i = 0 \tag{25}$$

Noting that the displacement and polarization vector fields are functions solely of the radial coordinate r, Eq. (25) transforms into:

$$W_r - \left(k^1 + \frac{\left(k^2 + k^3\right) k^4}{\tilde{\chi}}\right)(\Delta W)_r = 0 \tag{26}$$

or in compact form:

$$\mathbf{W} - \tilde{k}(\Delta \mathbf{W}) = 0 \tag{27}$$

where

$$\tilde{k} = \left(k^1 + \frac{\left(k^2 + k^3\right) k^4}{\tilde{\chi}}\right) \tag{28}$$

Given that the vector $\mathbf{W}$ represents the gradient of a scalar function ψ, expressed as $\mathbf{W} = \nabla\,\psi$, Eq. (27) leads with a direct integration to the modified Helmholtz equation:

$$\Delta\psi - k\psi = \mathcal{C} \tag{29}$$

where $k = 1/\tilde{k}$ and $\mathcal{C}$ an integration constant. However, in the framework of cylindrical coordinates, Eq. (29) can be reformulated as follows:

$$\Delta\psi = \frac{1}{r}(r\psi')' = \psi'' + \frac{\psi'}{r} \tag{30}$$

where the symbols $'$ and $''$ represent the derivatives $d(\cdot)/dr$ and $d^2(\cdot)/dr^2$, respectively. By setting the integration constant $\mathcal{C}$ in Eq. (30) to zero, we obtain the modified Bessel differential equation of order zero:

$$\psi'' + \frac{\psi'}{r} - k\psi = 0 \tag{31}$$

One can find the general solution to Eq. (31), as, e.g., in [53], by

$$\psi(r) = AI_0(\sqrt{k}r) + BK_0(\sqrt{k}r), \quad \text{and} \quad \mathrm{W} \equiv W_r = \psi' \tag{32}$$

where A and B are constants to be determined, while I_0 and K_0 are the modified Bessel functions of the first and second kinds of zero order, respectively.

Finally, the radial displacement, denoted as $U_r \equiv U$, is derived from the following differential equation:

$$W \equiv W_r = (\nabla \mathrm{tr}\,\mathbf{D})_r = (\mathrm{tr}\,\mathbf{D})_{,r} = \left(U' + \frac{U}{r}\right)' \tag{33}$$

Utilizing Eq. (33) and expressing W through ψ, followed by a direct integration, we can reformulate:

$$\left(U' + \frac{U}{r}\right)' = \psi' \quad \Rightarrow \quad (r\,U)' = AI_0(\sqrt{k}r)\,r + BK_0(\sqrt{k}r)\,r + \gamma\,r \tag{34}$$

being γ a constant of integration. Consequently, we derive explicitly:

$$r\,U(r) = D_1 \int I_0(\sqrt{k}r) r\,\mathrm{d}r + D_2 \int K_0(\sqrt{k}r) r\,\mathrm{d}r + D_3 r^2 + C_4 \tag{35}$$

or, in other words,

$$U(\rho) = D_1 I_1(\rho) + D_2 K_1(\rho) + D_3\rho + \frac{D_4}{\rho} \tag{36}$$

where $\rho = \sqrt{k}r$, with the constants D_i (where $i = \{1, 2, \ldots, 4\}$) determined by the boundary conditions of the problem. The functions I_1 and K_1 correspond to the modified Bessel functions of the first and second kinds of order one, respectively.

After obtaining the displacement field, we determine the polarization vector $P \equiv P_r$ by employing Eq. $(24)_2$; thus, we obtain

$$P = \frac{k^4}{\tilde{\chi}} W = \frac{k^4}{\tilde{\chi}} \psi' \tag{37}$$

and, therefore, we have:

$$P \equiv P(\rho) = A_1 I_1(\rho) - A_2 J_1(\rho) \tag{38}$$

where A_i (for $i = \{1, 2\}$) are the integration constants, J_1 is the Bessel function of the first kind of order one.

The solution of the electrical potential can easily be worked out using Eq. $(9)_3$ whose solution is given by

$$\Phi(\rho) = B_1 I_0(\rho) - B_2 J_0(\rho) + B_3$$

where B_i (for $i = \{1, 2, 3\}$) represents three integration constants, J_0 is the Bessel function of the first kind of zero order.

In summary, the analytical formulas for displacement, polarization, and electric potential fields pertaining to the problem analyzed are presented as follows:

$$\begin{cases} U(\rho) = D_1 I_1(\rho) + D_2 K_1(\rho) + D_3\rho + \dfrac{D_4}{\rho} \\ P(\rho) = A_1 I_1(\rho) - A_2 J_1(\rho) \\ \Phi(\rho) = B_1 I_0(\rho) - B_2 J_0(\rho) + B_3 \end{cases} \tag{39}$$

being A_i, B_i, and D_i constants of integration, determined by the selected boundary conditions. The constants of integration D_i can be determined by the conditions $U(r_i)$, $U(r_e)$, $\partial_r U(r_i)$, and $\partial_r U(r_e)$. The integration constants, denoted as A_i, in the polarization field vector expression can be determined by specifying the values of $P(r_i)$ and $P(r_e)$ on the inner and outer surfaces of the cylindrical tube, respectively. In recent work, the authors and others have applied similar conditions on both displacement and polarization fields to analytically address a closely related boundary value problem, as discussed in [27] and [9]. The integration constants, B_i, can be determined by considering the potential at the cylinder inner and outer surfaces, specifically $\Phi(r_i) = 0$ and $\Phi(r_e) = V$. Two of the three integration constants will be provided in this way; naturally, the last constant, B_3, can be set to zero. The proposed model and its corresponding closed-form solution raise several interesting points, as outlined in the following.

An important observation is that the displacement field, polarization, and electric potential are notably altered due to the influence of flexoelectric effects. Without the influence of flexoelectric effects, the SGE solution for the identical problem is obtained once again. Moreover, Eq. $(39)_1$ illustrates that incorporating flexoelectric effects within the model diminishes the displacement vector magnitude compared to both the classical and the SGE solutions. The reasoning is that a portion of the energy produced by external forces acting on the flexoelectric material has been utilized to polarize the cylindrical tube. Consequently, due to flexoelectric influences, the circumfacial strain $D_{\theta\theta}$ is significantly reduced compared to its magnitude in standard elastic and strain gradient elasticity scenarios. Moreover, the slope reflecting the change in radial strain D_{rr} due to flexoelectric effects is gently evened out.

Unlike the scenario with the SGE solution, when the strain gradient material constants c_i (for $i = \{1, 2, \ldots, 5\}$) vanish, the hyperstress M_{ijk} remains non-zero and is given by $K_{ijkl}P_l$. Consequently, this term influences polarization in a manner similar to the external electric vector field $\mathbf{E}^0$. Sometimes referred to as the flexoelectric field, this term is usefully introduced when examining the intensity of flexoelectric poling effects. This implies that even without an external electrical source, the tube is still able to become polarized due to the non-uniform deformation (strain gradient) it experiences. This occurs with any kind of materials, whether they are piezoelectric or not. Therefore, the polarization of the cylindrical tube can be modified by altering the mechanical loading settings, specifically by adjusting the specified displacement $U(r_{i,e})$ and/or the variation in displacement $\partial_r U(r_{i,e})$ on the inner and outer surfaces of the tube. In addition, mechanical external loading can regulate the local electrical behavior, even when there is no external electrical power present.

4 Illustration of the flexoelectric response

The most straightforward internal energy density W for a flexoelectric material that lacks piezoelectric properties can be represented as:

$$W = \frac{1}{2}C_{ijkl}D_{ij}D_{kl} + \frac{1}{2}H_{ijklmn}D_{ij,k}D_{lm,n} + \frac{1}{2}\chi_{ij}P_iP_j + K_{ijkl}P_iD_{jk,l}, \tag{40}$$

when some of the terms in Eq. (1) vanish.

The governing equations for the flexoelectric nanowire in cylindrical coordinates are given by:

$$\begin{cases} U(\tilde{\rho}) = D_1 I_1(\tilde{\rho}) + D_2 K_1(\tilde{\rho}) + D_3\tilde{\rho} + \dfrac{D_4}{\tilde{\rho}} \\ P(\tilde{\rho}) = A_1 I_1(\tilde{\rho}) - A_2 J_1(\tilde{\rho}) \\ \Phi(\tilde{\rho}) = B_1 I_0(\tilde{\rho}) - B_2 J_0(\tilde{\rho}) + B_3 \end{cases} \tag{41}$$

where $\tilde{\rho} = \dfrac{\rho}{\sqrt{k}r_e}$ is the dimensionless radial coordinate, and I_n and K_n are Bessel functions of the first and second kind.

The next section details the numerical solution and analysis of a system of coupled equations involving displacement $U(\tilde{\rho})$, pressure $P(\tilde{\rho})$, and potential $\Phi(\tilde{\rho})$ in cylindrical coordinates. These functions are governed by combinations of Bessel functions and linear terms, with boundary conditions specified for their values and derivatives. The study investigates the mathematical, physical, and mechanical implications of the solutions.

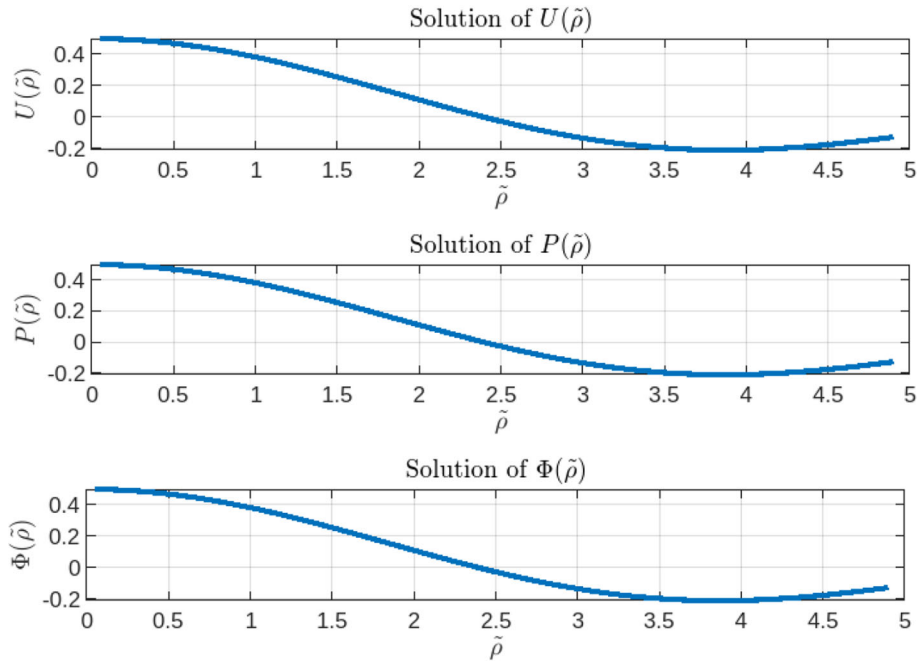


Fig. 3 Solutions $U(r)$, $P(r)$, and $\Phi(r)$ over the domain r

4.1 Implementation

The equations were discretized in the domain $r \in [r_{\min}, r_{\max}]$, with $r_{\min} = 0.1$ and $r_{\max} = 10$. The boundary conditions applied were as follows:

$$\begin{aligned} U(\tilde{\rho}_{\min}) &= U_{\min}, \quad U'(\tilde{\rho}_{\max}) = U'_{\max}, \\ P(\tilde{\rho}_{\min}) &= P_{\min}, \quad P(\tilde{\rho}_{\max}) = P_{\max}, \\ \Phi(\tilde{\rho}_{\min}) &= \Phi_{\min}, \quad \Phi(\tilde{\rho}_{\max}) = \Phi_{\max}. \end{aligned}$$

The constants associated with the equations were determined using the MATLAB optimization tool `fsolve`, ensuring the boundary conditions were satisfied. The results were evaluated using 1000 discretization points for smooth and accurate solutions.

4.2 Results and discussion

4.2.1 Mathematical perspective

The solutions for $U(\tilde{\rho})$, $P(\tilde{\rho})$, and $\Phi(\tilde{\rho})$ exhibit the expected behavior of Bessel functions. The exponential growth of $I_n(\tilde{\rho})$ and decay of $K_n(\tilde{\rho})$ are apparent, and the oscillatory nature of $J_n(\tilde{\rho})$ aligns with theoretical predictions. The interaction of linear terms with Bessel functions smooths the transition between boundary conditions (Fig. 3).

4.2.2 Physical perspective

Physically, $U(\tilde{\rho})$ can represent displacement in a cylindrical structure, $P(\tilde{\rho})$ pressure, and $\Phi(\tilde{\rho})$ potential. The boundary conditions simulate realistic constraints such as fixed displacement and stress gradients at the edges.

The solutions indicate:

- Displacement increases linearly in regions dominated by $D_3\tilde{\rho}$,
- Stress gradients change smoothly across the domain,
- Energy density peaks near the boundaries due to higher deformation (Figs. 4, 5).

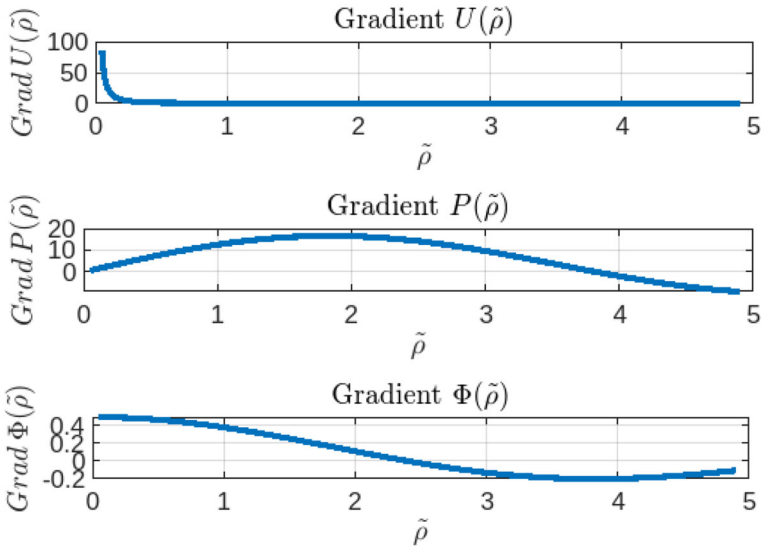


Fig. 4 Solutions $U(\tilde{\rho})$, $P(\tilde{\rho})$, and $\Phi(\tilde{\rho})$ over the domain $\tilde{\rho}$

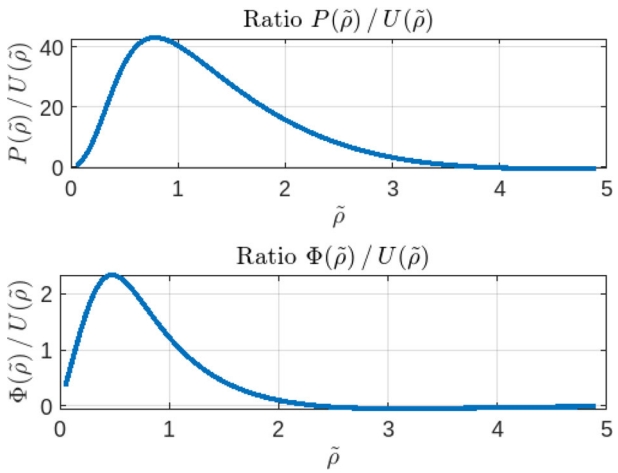


Fig. 5 Ratios $P(\tilde{\rho})/U(\tilde{\rho})$ and $\Phi(\tilde{\rho})/U(\tilde{\rho})$ over the domain $\tilde{\rho}$

4.2.3 Mechanics Perspective

Mechanically, $U'(\tilde{\rho})$ reflects strain distribution, which transitions smoothly due to the coupling between linear and Bessel terms. The pressure $P(\tilde{\rho})$ captures compressive or tensile states, and $\Phi(\tilde{\rho})$ shows the distribution of scalar potential, which could relate to stress or energy fluxes in materials.

The energy density $E(\tilde{\rho}) = \frac{1}{2}U(\tilde{\rho})^2$ increases near the boundary (Fig. 6), suggesting regions of significant deformation. These insights are critical for understanding the mechanical stability of the structure under external loads.

4.2.4 Boundary Conditions Validation

The numerical solution was validated against the imposed boundary conditions. The plots confirm the satisfaction of the specified values and derivatives at the boundaries, ensuring the reliability of the results.

The numerical implementation and analysis reveal the interplay between mathematical solutions, physical properties, and mechanical behavior in cylindrical systems. The results align with theoretical expectations, demonstrating smooth transitions and realistic boundary conditions. Future work could involve incorporating nonlinearity or external forces for more complex models.

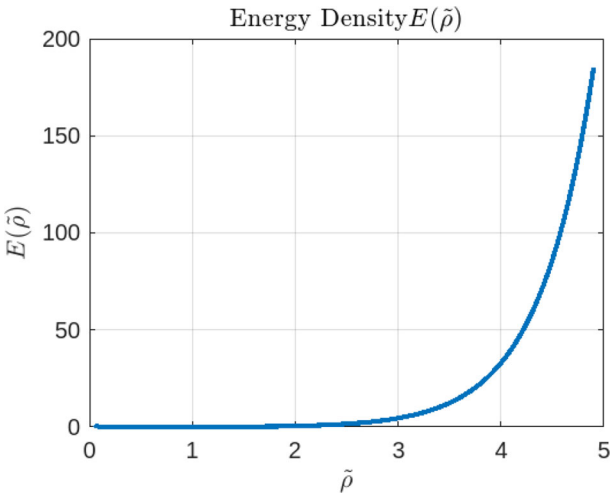


Fig. 6 Energy density $E(\tilde{\rho}) = \frac{1}{2}U(\tilde{\rho})^2$ over the domain $\tilde{\rho}$

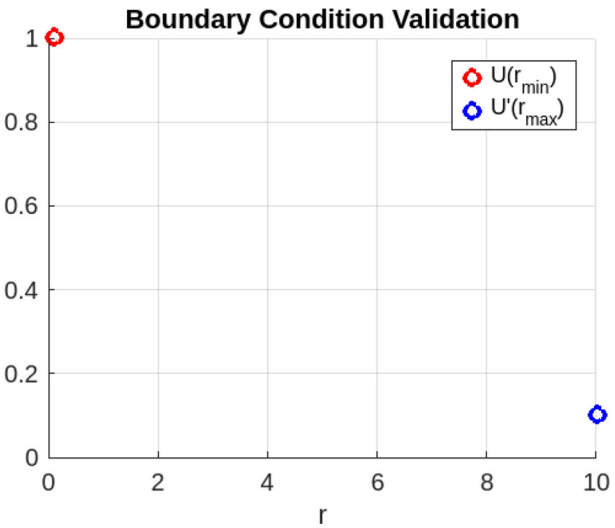


Fig. 7 Validation of boundary conditions for $U(r)$ and $U'(r)$ at the boundaries

4.3 Analysis of the results with flexoelectric effects

In this section, we present the results obtained by incorporating flexoelectric effects into the analysis. The inclusion of these effects modifies the response of the material, especially under strain gradients, leading to notable changes in both mechanical and electrical behavior. We focus on how these effects influence the performance of the system in the context of the specific conditions studied (Fig. 7).

The results demonstrate a clear impact of flexoelectric coupling, with significant variations observed in the system's properties. These findings highlight the importance of accounting for flexoelectric effects to better understand and predict the material behavior under varying mechanical loads and electric fields.

For this numerical experiment, we used the ZnO material to investigate the influence of flexoelectric effects. The properties of ZnO, including its flexoelectric and dielectric characteristics, are crucial for the simulation and are accounted for in the analysis. These properties significantly affect the material response under mechanical stress and electric fields, making it an ideal candidate for studying the flexoelectric behavior.

The material parameters used in the simulations are summarized in Table 1. To determine the coefficients of the material strain gradient, c_1, c_2, c_3, c_4, and c_5, we employed the formalism outlined in [29], which provides a systematic methodology for strain gradient elasticity. This formalism maps an earlier strain gradient model onto the one developed by Enakoutsa and Leblond [31], where the strain gradient elasticity framework incorporates

Table 1 Material parameters of the Zinc oxide (ZnO) used in the calculations.

Property	Value
E (Young's modulus)	129 GPa
ν (Poisson's ratio)	0.349
k_{12}	10^{-9} C m^{-1}
k_{44}	10^{-9} C m^{-1}
d_{12}	110.4 GPa
d_{44}	47.83 GPa
a	0
χ	10^{-9} C m^{-1}
b_{12}	0
b_{44}	0

Lamé's moduli. The process begins with the governing equations:

$$\begin{aligned}
\frac{c_1}{(1-f)(b^2/5)} &= -\frac{\lambda}{4}, \\
\frac{c_2}{(1-f)(b^2/5)} &= \lambda, \\
\frac{c_3}{(1-f)(b^2/5)} &= \frac{\lambda}{16} - \frac{\mu}{4}, \\
\frac{c_4}{(1-f)(b^2/5)} &= \mu, \\
c_5 &= 0,
\end{aligned}$$

We substituted the known values[1] $b = 1$, $f = 0$, $\lambda = 110.4\,\text{GPa}$, and $\mu = 47.83\,\text{GPa}$. Using these inputs, the coefficients were calculated as:

$$\begin{aligned}
c_1 &= -5.52\,\text{GPa}, & c_2 &= 22.08\,\text{GPa}, & & \\
c_3 &= -1.012\,\text{GPa}, & c_4 &= 9.566\,\text{GPa}, & c_5 &= 0.
\end{aligned}$$

Using these coefficients, the values of k^1, k^2, k^3 and k^4 were determined. Specifically, k^1 was computed as:

$$k^1 = \frac{4c_1 + c_2 + 4c_3 + 2c_4}{\lambda + 2\mu} \approx 0.0732.$$

The values of k^2 and k^3 were found to be in the order of 10^{-21}, given the small magnitude of the constants k_{12} and k_{44}. k^4 was calculated as 206.06 GPa. Finally, the expression $k^1 + \frac{(k^2+k^3)k^4}{\lambda+2\mu}$ was evaluated, where the additional term contributed negligibly due to the smallness of $k^2 + k^3$, resulting in an overall value dominated by k^1.

Figures 8, 9, 10, and 11 are analogous to Figures 3, 4, 5, and 6, but with the inclusion of flexo-electric effects, which were not considered in the corresponding figures. The primary difference between the two sets of figures lies in the noticeable changes in the displacement, polarization, and electrical field profiles.

In the absence of flexo-electricity, as shown in Figures 3, 4, and 5, the displacement and polarization fields exhibit sinusoidal shapes, reflecting a periodic response of the system to external stimuli (such as

[1] The simplifications $f = 0$ and $b = 1$ are applied as part of the initial calibration of the model to establish a baseline for analysis. Setting $f = 0$ assumes a fully dense material without voids, simplifying the problem by eliminating the complexities introduced by porosity. This allows calibration to focus solely on intrinsic material properties under idealized conditions. Once the model is validated, the effect of porosity ($f > 0$) can be reintroduced to study its impact. Similarly, setting $b = 1$, which corresponds to normalizing the characteristic length scale, simplifies the governing equations by making them dimensionless. This normalization eliminates scaling factors and provides a clear relationship between the material coefficients (c_1, c_2, c_3, c_4, c_5) and the Lamé parameters (λ, μ). After initial calibration, realistic values of b can be incorporated to reflect microstructural characteristics. These assumptions create an ideal starting point for the model, ensuring that it behaves as expected under simplified conditions. This baseline serves as a reference framework for systematically incorporating additional complexities, such as porosity and microstructural effects, in later stages.

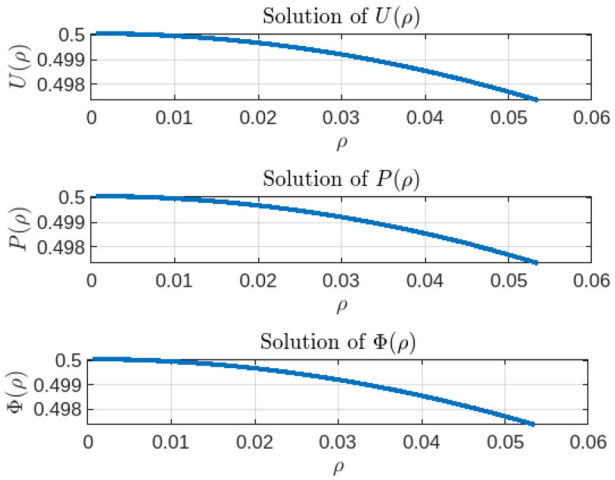


Fig. 8 Solutions $U(\rho)$, $P(\rho)$, and $\Phi(\rho)$ over the domain ρ

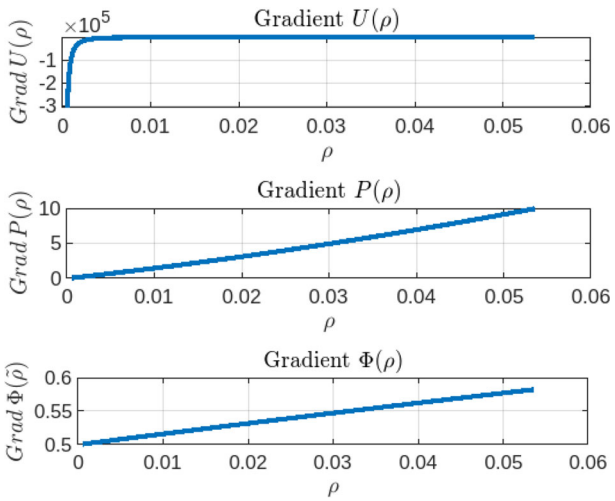


Fig. 9 Solutions $U(\rho)$, $P(\rho)$, and $\Phi(\rho)$ over the domain ρ

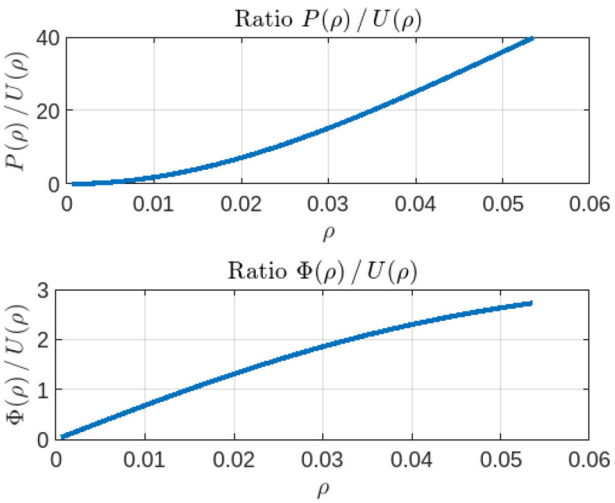


Fig. 10 Ratios $P(\rho)/U(\rho)$ and $\Phi(\rho)/U(\rho)$ over the domain ρ

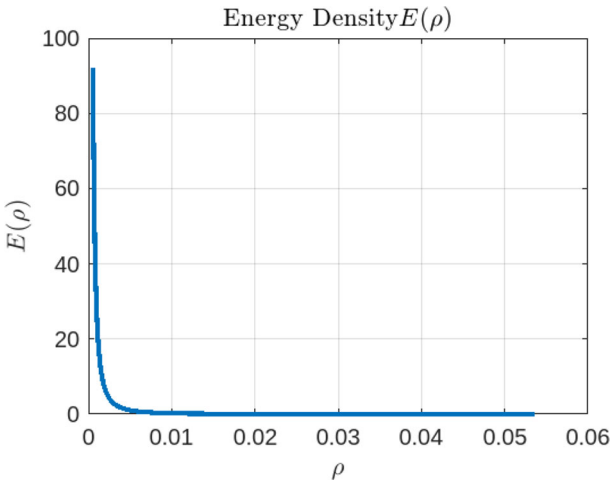


Fig. 11 Energy density $E(\rho) = \frac{1}{2}U(\rho)^2$ over the domain ρ

mechanical deformation or electric fields). These sinusoidal variations arise from the interplay between the applied forces and the intrinsic material properties, where the polarization is typically aligned or anti-aligned with the displacement in a straightforward manner.

However, when flexoelectricity is included, as shown in Figs. 8, 9, and 10, the sinusoidal pattern is altered. The flexoelectric effect introduces a coupling between the mechanical deformation (displacement) and the polarization (electric field), leading to a more complex response. Flexoelectricity, a phenomenon that links strain gradients to electric polarization, introduces additional terms in the governing equations that affect the field distributions.

This coupling modifies the symmetry of the displacement and polarization fields. Instead of maintaining a simple sinusoidal pattern, the fields may become non-periodic or exhibit altered periodicities, reflecting the additional influence of mechanical strain gradients on the electric field. In particular, flexoelectricity tends to induce polarization even in the absence of an external electric field, and this can lead to shifts in the electric potential distribution, changing the shape and intensity of the electrical fields.

Furthermore, the energy density plot, shown in Fig. 11, further supports this observation. In the absence of flexoelectricity, the energy density curve increases, reflecting the increase in energy as a result of applied mechanical deformation and electrical fields. In contrast, when flexoelectricity is included, the energy density curve decreases. This reduction suggests that the flexoelectric coupling influences the system in such a way that energy is dissipated or redistributed differently compared to the case without flexoelectricity. The presence of flexoelectric effects may lead to more efficient energy redistribution or even the storage of energy in a manner that contrasts with a simpler, purely mechanical system.

In general, these differences in behavior highlight the impact of flexoelectricity on the response of the system, altering the distribution and symmetry of the mechanical and electrical fields. This coupling is crucial in materials that exhibit both piezoelectric and flexoelectric properties, where the interplay between strain gradients and electric polarization significantly affects the material's overall behavior, especially under varying mechanical or electrical loads.

5 Size effects analysis of the analytic solution

As the dimensions of materials shrink to the nanoscale, their mechanical and electromechanical properties often deviate significantly from bulk behavior. Nanowires, with their high surface-to-volume ratio and reduced dimensionality, exhibit pronounced size-dependent effects that are not adequately captured by classical continuum theories. One such phenomenon is *flexoelectricity*—the coupling between strain gradients and electric polarization—which becomes increasingly significant at small scales due to the enhanced strain gradients inherent in nanoscale structures.

Traditional continuum mechanics models typically consider only the first-order strain and neglect higher-order gradients and their associated boundary conditions. Although this simplification is acceptable for bulk

materials, it falls short when applied to nanowires, where the characteristic length scale L is comparable to the material's internal length scales associated with higher-order effects. In such cases, the *strain gradients* can no longer be considered negligible, and their contributions to the material response must be explicitly accounted for.

The necessity of a higher-order theory arises from the scaling behavior of strain gradients and their influence on the internal energy density of the material. Specifically:

- **Strain gradients** scale inversely with the characteristic length of the nanowire, $\sim 1/L$, leading to energy contributions that scale as $\sim 1/L^2$.
- **Higher-order strain gradients**, such as the second derivatives of displacement, scale as $\sim 1/L^2$, contributing terms that scale as $\sim 1/L^4$.

5.1 Analytical solutions

The derived solutions for the radial displacement $U(\tilde{\rho})$, polarization $P(\tilde{\rho})$, and electric potential $\Phi(\tilde{\rho})$ are expressed in terms of modified Bessel functions. These solutions reflect the complexity of higher-order gradient theories and include coefficients that depend on material properties, geometric parameters, and boundary conditions. The general forms of the solutions are:

$$U(\tilde{\rho}) = D_1 I_1(\tilde{\rho}) + D_2 K_1(\tilde{\rho}) + D_3\tilde{\rho} + \frac{D_4}{\tilde{\rho}}, \tag{42}$$

$$P(\tilde{\rho}) = A_1 I_1(\tilde{\rho}) - A_2 J_1(\tilde{\rho}), \tag{43}$$

$$\Phi(\tilde{\rho}) = B_1 I_0(\tilde{\rho}) - B_2 J_0(\tilde{\rho}) + B_3, \tag{44}$$

where $I_n(\tilde{\rho})$ and $K_n(\tilde{\rho})$ are modified Bessel functions of the first and second kinds, and $J_n(\tilde{\rho})$ is the Bessel function of the first kind. The coefficients D_i, A_i, B_i are determined by the imposed boundary conditions and depend on material properties such as elastic and flexoelectric constants.

5.2 Boundary conditions and coefficient dependencies

The coefficients D_i, A_i, B_i are derived by imposing boundary conditions:

- Displacement: $U(\tilde{\rho}_{\text{inner}}) = U_{\text{inner}},\ U(\tilde{\rho}_{\text{outer}}) = U_{\text{outer}}$,
- Polarization: $P(\tilde{\rho}_{\text{inner}}) = P_{\text{inner}},\ P(\tilde{\rho}_{\text{outer}}) = P_{\text{outer}}$,
- Electric Potential: $\Phi(\tilde{\rho}_{\text{inner}}) = \Phi_{\text{inner}},\ \Phi(\tilde{\rho}_{\text{outer}}) = \Phi_{\text{outer}}$.

These coefficients encapsulate material properties, including elastic constants (E, ν), flexoelectric constants (μ), and dielectric constants (ϵ), as well as geometric parameters such as characteristic length L and radii $\tilde{\rho}_{\text{inner}}, \tilde{\rho}_{\text{outer}}$.

5.3 Asymptotic behavior

The analytical solutions exhibit distinct behaviors at small and large scales, emphasizing the size-dependent effects:

Small-Scale Behavior $(\tilde{\rho} \to 0)$ For small values of $\tilde{\rho}$, the asymptotic expansions of the modified Bessel functions are:

$$I_n(\tilde{\rho}) \sim \frac{(\tilde{\rho}/2)^n}{\Gamma(n+1)}, \tag{45}$$

$$K_n(\tilde{\rho}) \sim \frac{\Gamma(n)}{2}\left(\frac{2}{\tilde{\rho}}\right)^n. \tag{46}$$

Using these approximations:

- Displacement $U(\tilde{\rho})$ is dominated by the inverse term $\frac{D_4}{\tilde{\rho}}$ and $K_1(\tilde{\rho})$, leading to steep strain gradients near the boundaries.

- Polarization $P(\tilde{\rho})$ is amplified near the inner boundary due to the dominance of $K_1(\tilde{\rho})$, which scales as $\frac{1}{\tilde{\rho}}$.
- Electric potential $\Phi(\tilde{\rho})$ depends strongly on the boundary conditions, with $J_0(\tilde{\rho})$ remaining finite as $\tilde{\rho} \to 0$.

Large-Scale Behavior ($\tilde{\rho} \to \infty$) For large values of $\tilde{\rho}$, the modified Bessel functions exhibit the following asymptotic behavior:

$$I_n(\tilde{\rho}) \sim \frac{e^{\tilde{\rho}}}{\sqrt{2\pi\tilde{\rho}}}, \tag{47}$$

$$K_n(\tilde{\rho}) \sim \sqrt{\frac{\pi}{2\tilde{\rho}}} e^{-\tilde{\rho}}. \tag{48}$$

At large scales:

- Displacement $U(\tilde{\rho})$ grows exponentially due to $I_1(\tilde{\rho})$, reflecting the increasing influence of higher-order terms.
- Polarization $P(\tilde{\rho})$ decays as the terms involving $J_1(\tilde{\rho})$ diminish.
- Electric potential $\Phi(\tilde{\rho})$ stabilizes or decays, depending on the contributions of $B_1 I_0(\tilde{\rho})$ and $B_2 J_0(\tilde{\rho})$.

6 Dimensionless parameters and size effects

The behavior of flexoelectric materials at the nanoscale is strongly influenced by size-dependent phenomena, which are captured through dimensionless parameters. These parameters quantify the relative importance of material properties, geometric dimensions, and higher-order gradient effects, providing critical insights into the scaling laws that govern mechanical and electromechanical responses.

Definition of dimensionless parameters

To analyze the size effects, the governing equations and analytical solutions are reformulated in terms of dimensionless variables. Let:

$$\tilde{\rho} = \frac{\rho}{L}, \quad \tilde{U} = \frac{U}{L}, \quad \tilde{P} = \frac{P}{P_0}, \quad \tilde{\Phi} = \frac{\Phi}{\Phi_0}, \tag{49}$$

where L is the characteristic length scale of the system, P_0 is a reference polarization, and Φ_0 is a reference electric potential. The dimensionless variables ensure that the solutions are independent of the absolute system size, highlighting scaling effects.

Dimensionless form of analytical solutions

Rewriting the analytical solutions in terms of the dimensionless parameters:

$$\tilde{U}(\tilde{\rho}) = \tilde{D}_1 I_1(\tilde{\rho}) + \tilde{D}_2 K_1(\tilde{\rho}) + \tilde{D}_3 \tilde{\rho} + \frac{\tilde{D}_4}{\tilde{\rho}}, \tag{50}$$

$$\tilde{P}(\tilde{\rho}) = \tilde{A}_1 I_1(\tilde{\rho}) - \tilde{A}_2 J_1(\tilde{\rho}), \tag{51}$$

$$\tilde{\Phi}(\tilde{\rho}) = \tilde{B}_1 I_0(\tilde{\rho}) - \tilde{B}_2 J_0(\tilde{\rho}) + \tilde{B}_3, \tag{52}$$

where $\tilde{D}_i$, $\tilde{A}_i$, $\tilde{B}_i$ are dimensionless coefficients that depend on the material constants, boundary conditions, and characteristic length L.

Scaling relationships

The dimensionless coefficients are influenced by material properties and geometric dimensions. For example:

- The strain gradient term $\nabla^2 U$ scales as $\sim \frac{1}{L^2}$, amplifying its contribution as L decreases.
- The polarization gradient term $\nabla^2 P$ scales as $\sim \frac{1}{L^3}$, becoming dominant at nanoscale dimensions.
- Flexoelectric coupling constants μ and higher-order constants α influence the relative strength of strain-induced polarization.

Size effects in the analytical solutions

The asymptotic behavior of the fields reveals the impact of size effects:

- **Small-scale effects** ($\tilde{\rho} \to 0$): At small length scales, terms involving inverse powers of $\tilde{\rho}$, such as $\frac{\tilde{D}_4}{\tilde{\rho}}$ and $K_1(\tilde{\rho})$, dominate. This results in:
  - Enhanced strain gradients, leading to amplified polarization near boundaries.
  - Steep electric potential gradients, influenced by localized polarization fields.
- **Large-scale effects** ($\tilde{\rho} \to \infty$): At large scales, exponential terms such as $I_1(\tilde{\rho})$ and $I_0(\tilde{\rho})$ dominate, while higher-order gradient effects diminish. This leads to:
  - Reduced coupling between mechanical and electromechanical fields.
  - Convergence to classical elasticity and electromechanics, where size-dependent phenomena are negligible.

Impact of dimensionless parameters on device performance

The dimensionless analysis provides key insights to optimize nanoscale devices: The energy harvesting efficiency is significantly influenced by the characteristic length scale L. Smaller L enhances energy conversion efficiency due to amplified strain and polarization gradients, which are critical for flexoelectric performance. However, reducing L to extremely small values may introduce material defects or structural instabilities, necessitating a balance between efficiency and durability.

For sensing applications, the sensitivity of flexoelectric sensors increases as L decreases. This is attributed to the more pronounced localization of polarization fields at smaller scales. By carefully tailoring L and optimizing material constants such as flexoelectric and dielectric properties, precise control over sensing performance can be achieved, enabling high-resolution detection capabilities.

Dimensionless parameters further highlight the scalability of device designs by establishing relationships between performance metrics, such as energy output and sensitivity, and system size and material properties. These relationships provide a systematic framework for optimizing device performance across various scales while maintaining efficiency and functionality.

7 Energy harvesting and sensing implications

The analytical framework developed in this study has significant implications for the design and optimization of energy harvesting and sensing devices. By leveraging size-dependent effects and higher-order gradient theories, flexoelectric materials can achieve enhanced performance in nanoscale applications. This section explores the practical relevance of the derived solutions and their impact on device efficiency and sensitivity.

7.1 Energy harvesting applications

Flexoelectric materials have shown great potential in energy harvesting, where mechanical deformation is converted into electrical energy. The coupling between strain gradients and polarization fields plays a critical role in determining energy conversion efficiency.

The efficiency of energy-harvesting devices is influenced by several critical factors. Strain gradients, represented by $\nabla^2 U$, scale as $\sim \frac{1}{L^2}$ and become more pronounced as the system size decreases. This amplification

of strain gradients leads to higher polarization gradients, which are essential for energy harvesting. The polarization field $P(\tilde{\rho})$, induced by these strain gradients, contributes directly to the electric displacement field and governs the generation of electric potential, forming the basis for energy conversion.

Electromechanical coupling plays a vital role in this process. Flexoelectric constants μ and higher-order terms α enhance the conversion of mechanical energy into electrical energy, particularly at nanoscale dimensions where gradient effects dominate. Additionally, geometric parameters, such as the aspect ratio of the device (e.g., length-to-thickness ratio), influence strain distribution and polarization fields, providing a pathway for optimizing energy output. These interconnected factors underline the importance of size effects and material properties in the design of efficient energy harvesting devices.

Analytical Insights for Optimization From the analytical solutions:

$$U(\tilde{\rho}) = D_1 I_1(\tilde{\rho}) + D_2 K_1(\tilde{\rho}) + D_3\tilde{\rho} + \frac{D_4}{\tilde{\rho}}, \tag{53}$$

$$P(\tilde{\rho}) = A_1 I_1(\tilde{\rho}) - A_2 J_1(\tilde{\rho}), \tag{54}$$

$$\Phi(\tilde{\rho}) = B_1 I_0(\tilde{\rho}) - B_2 J_0(\tilde{\rho}) + B_3, \tag{55}$$

the coupling between $\nabla^2 U$, $P(\tilde{\rho})$, and $\Phi(\tilde{\rho})$ reveals that reducing L enhances polarization gradients, increasing the electric field $\nabla\Phi$. However, extreme miniaturization must balance:

- **Enhanced Output:** Higher gradients produce larger electric fields and energy densities.
- **Structural Limitations:** Excessive strain gradients can lead to material degradation or instability.

Applications in Energy Harvesters Examples of practical applications of flexoelectric materials in energy harvesting include cantilever-based harvesters, thin film devices, and multi-layered structures. Cantilever-based harvesters use mechanical bending to generate strain gradients, which are then converted into electrical energy. In such devices, flexoelectric nanowires are embedded either on the surface or within the structure to maximize energy output.

Thin film devices represent another prominent application. These systems leverage compressive or tensile loading to produce localized strain gradients within the thin film. This results in significant polarization and energy generation, making them ideal for integration into compact and scalable energy systems.

Finally, multi-layered structures offer a highly efficient approach to energy harvesting. By combining layers of flexoelectric materials with carefully optimized thickness and density, these structures amplify the cumulative polarization and electric potential, thereby enhancing the overall energy harvesting performance. Such configurations are particularly well-suited for applications requiring high energy output from limited mechanical inputs.

7.1.1 Cantilever-based energy harvester

A concrete application of the derived analytical solutions is a cantilever-based energy harvester embedded with flexoelectric nanowires. This setup exploits mechanical bending to induce strain gradients, which generate electrical energy through the flexoelectric effect.

System description The cantilever beam is modeled as a rectangular structure of length L_b, width W_b, and thickness T_b. Flexoelectric nanowires are embedded or coated along the beam, with each nanowire characterized by length L_n and radius R_n. When subjected to a tip deflection δ, the cantilever generates a mechanical strain gradient that induces polarization and electric potential fields.

Analytical representation of energy harvesting Using the derived displacement field:

$$U(\tilde{\rho}) = D_1 I_1(\tilde{\rho}) + D_2 K_1(\tilde{\rho}) + D_3\tilde{\rho} + \frac{D_4}{\tilde{\rho}},$$

the radial strain gradient is given by:

$$\epsilon_{rr} = \frac{\partial U}{\partial \tilde{\rho}} = D_1 I_1'(\tilde{\rho}) + D_2 K_1'(\tilde{\rho}) + D_3 - \frac{D_4}{\tilde{\rho}^2}.$$

The strain gradient ϵ_{rr} induces polarization via the flexoelectric relation:

$$P(\tilde{\rho}) = \mu\nabla\epsilon_{rr} + \alpha\nabla^2\epsilon_{rr},$$

Table 2 Material and Geometric Parameters Representative of $BaTiO_3$ Nanowire-Based Cantilever, [70,83]

Property	Value
L_b	10 mm
W_b	2 mm
T_b	0.5 mm
L_n	50 nm
R_n	10 nm
μ	1 nC/m (Flexoelectric constant)
δ	1 mm (Tip deflection)

where μ and α are the flexoelectric and higher-order coupling constants, respectively. Substituting the strain gradient terms, we find:

$$P(\tilde{\rho}) = \mu \left(D_1 I_1''(\tilde{\rho}) + D_2 K_1''(\tilde{\rho}) - \frac{2D_4}{\tilde{\rho}^3} \right) + \alpha \nabla^2 \epsilon_{rr}.$$

The polarization $P(\tilde{\rho})$ contributes to the electric displacement field, which generates the potential:

$$\Phi(\tilde{\rho}) = B_1 I_0(\tilde{\rho}) - B_2 J_0(\tilde{\rho}) + B_3.$$

Energy output estimation The energy output $E_{\text{harvested}}$ is determined by integrating the electric field $-\nabla\Phi(\tilde{\rho})$ over the active volume of the device:

$$E_{\text{harvested}} = \int_V (-\nabla\Phi(\tilde{\rho}) \cdot \mathbf{D})\, dV,$$

where $\mathbf{D} = \epsilon \mathbf{E} + P$ is the electric displacement field.

For a cantilever with flexoelectric nanowires:

$$E_{\text{harvested}} \sim \frac{\mu^2}{L_n^3} \int_0^{L_b} \int_0^{W_b} \left[I_1'(\tilde{\rho})^2 + K_1'(\tilde{\rho})^2 \right] dx\, dy. \tag{56}$$

This shows that the energy output increases with decreasing L_n due to improved strain gradients.

Case study parameters Consider a cantilever with the parameters given in Table 2.

The numerical integration of the derived equations yields an energy output of approximately $E_{\text{harvested}} = 2.5\,\mu$J per cycle, demonstrating the feasibility of flexoelectric-based energy harvesters. The material parameters used in this example are representative of Barium Titanate ($BaTiO_3$) nanowires, a well-characterized flexoelectric ceramic commonly used in nanoscale energy harvesting devices due to its moderate flexoelectric coefficient and favorable mechanical-electrical coupling properties [70,83].

Design insights The results highlight several important design considerations:

Nanowire density: Increasing the density of embedded nanowires improves energy output, as strain gradients are distributed over a larger active area.

Device size: Smaller L_n amplifies strain gradients, but care must be taken to avoid structural instabilities.

Material properties: Higher flexoelectric constants (μ) and dielectric properties (ϵ) lead to improved energy harvesting performance.

7.1.2 Thin film devices

A thin film flexoelectric device provides a practical application of the derived analytical solutions for energy harvesting. Thin films, when subjected to compressive or tensile stresses, generate strain gradients that induce polarization and electric fields, enabling energy harvesting through the flexoelectric effect.

System description Consider a thin film of thickness t_f, length L_f, and width W_f, attached to a rigid substrate. When a uniaxial compressive or tensile stress σ_x is applied along the length, a strain gradient develops through the thickness of the film. The strain gradient induces polarization, generating an electric potential difference across the film.

Analytical representation of thin film energy harvesting The displacement field in the film, under the assumption of plane strain conditions, is given by:

$$U(\tilde{\rho}) = D_1 I_1(\tilde{\rho}) + D_2 K_1(\tilde{\rho}) + D_3 \tilde{\rho} + \frac{D_4}{\tilde{\rho}},$$

where $\tilde{\rho} = \frac{\rho}{t_f}$ is the dimensionless thickness coordinate. The strain gradient in the thickness direction is:

$$\epsilon_{rr} = \frac{\partial U}{\partial \tilde{\rho}} = D_1 I_1'(\tilde{\rho}) + D_2 K_1'(\tilde{\rho}) + D_3 - \frac{D_4}{\tilde{\rho}^2}.$$

The induced polarization $P(\tilde{\rho})$ is determined by:

$$P(\tilde{\rho}) = \mu \nabla \epsilon_{rr} + \alpha \nabla^2 \epsilon_{rr},$$

where μ and α are the flexoelectric and higher-order coupling constants, respectively. Substituting the strain gradient terms:

$$P(\tilde{\rho}) = \mu \left(D_1 I_1''(\tilde{\rho}) + D_2 K_1''(\tilde{\rho}) - \frac{2D_4}{\tilde{\rho}^3} \right) + \alpha \nabla^2 \epsilon_{rr}.$$

The electric potential difference $\Delta\Phi$ across the film is obtained from the polarization field:

$$\Delta\Phi = \int_0^{t_f} \frac{P(\tilde{\rho})}{\epsilon} \, d\tilde{\rho},$$

where ϵ is the dielectric constant of the material.

Energy output estimation The harvested energy $E_{\text{harvested}}$ from the thin film is calculated as:

$$E_{\text{harvested}} = \frac{1}{2} C \Delta\Phi^2,$$

where C is the capacitance of the thin film, given by:

$$C = \frac{\epsilon W_f L_f}{t_f}.$$

Substituting for $\Delta\Phi$:

$$E_{\text{harvested}} \sim \frac{\mu^2}{t_f^3} \int_0^{t_f} \left[I_1''(\tilde{\rho})^2 + K_1''(\tilde{\rho})^2 \right] d\tilde{\rho}.$$

Case study parameters Consider a thin film with the following parameters:

Numerical evaluation yields:

$$\Delta\Phi \approx 0.5\,\text{V}, \quad E_{\text{harvested}} \approx 1.2\,\mu\text{J}.$$

Further results and discussion

The impact of size effects on energy harvesting efficiency in flexoelectric materials is a critical aspect of nanoscale energy conversion. The following figures provide key insights into how flexoelectricity influences energy generation in thin-film devices. By examining (1) Energy Output vs. Flexoelectric Constant, (2) Energy Harvesting Efficiency vs. Film Thickness, and (3) Electric Potential Difference vs. Film Thickness, we gain a deeper understanding of how flexoelectricity can be optimized for practical applications.

Figure 12 illustrates the energy output as a function of the flexoelectric constant. The quadratic dependence of energy output on the flexoelectric constant suggests that materials with higher flexoelectric coefficients exhibit significantly enhanced energy conversion efficiency. This aligns with previous studies that demonstrate that the flexoelectric effect becomes dominant in nanoscale structures where strain gradients are pronounced [69].

Furthermore, this result suggests that material engineering strategies that focus on increasing the flexoelectric response (e.g., by defect engineering, strain tuning, or layered heterostructures) can be used to enhance performance. Compared to traditional piezoelectric materials, which require non-centrosymmetric crystal structures, flexoelectricity provides an advantage as it is present in all dielectric materials, making it broadly applicable to energy harvesting technologies.

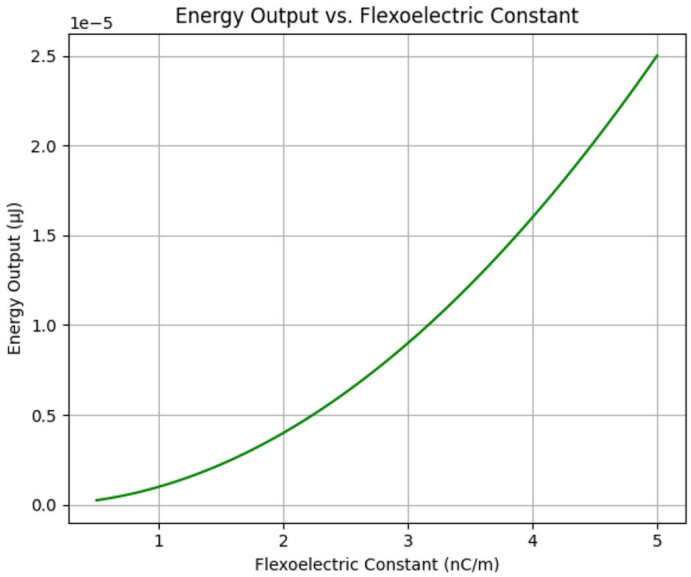


Fig. 12 Energy output as a function of the flexoelectric constant, exhibiting a clear quadratic dependence

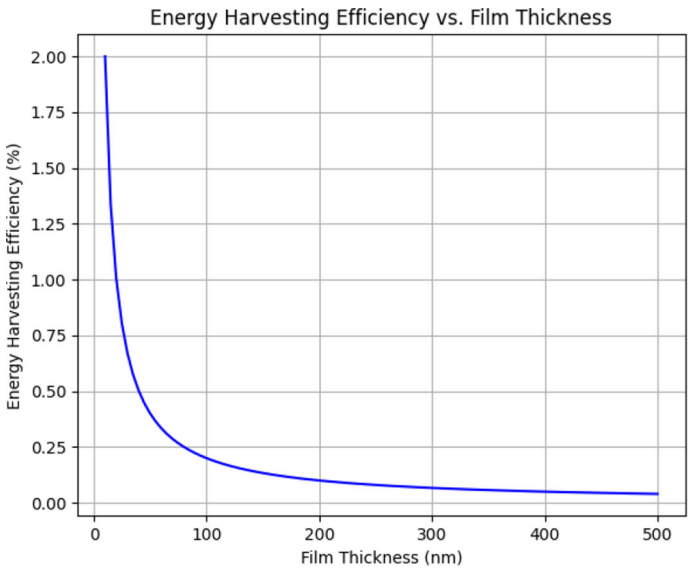


Fig. 13 Energy harvesting efficiency as a function of film thickness, illustrating an inverse relationship–efficiency increases significantly as the film becomes thinner due to enhanced strain gradients

Figure 13 highlights the inverse relationship between energy harvesting efficiency and film thickness. As the film thickness decreases, the efficiency increases sharply, particularly below 100 nm. This behavior is consistent with theoretical models that predict the flexoelectric effect to be enhanced in ultrathin films due to increased strain gradients [76]. However, this trend also implies that for films thinner than 10 nm, additional factors such as leakage currents, increased surface roughness, and quantum mechanical effects may become limiting factors.

Comparing this result with similar studies on piezoelectric nanogenerators, it is evident that flexoelectric energy harvesters provide a unique advantage in sub-100 nm regimes, where conventional piezoelectric materials suffer from size-induced property degradation. Moreover, ultra-thin film flexoelectric harvesters are advantageous for applications requiring flexible, high-efficiency, and low-power devices, such as self-powered sensors and biomedical implants.

Figure 14 shows the difference in the electric potential as a function of the thickness of the film. The strong increase in electric potential for thinner films is indicative of enhanced polarization as a result of flexoelectricity.

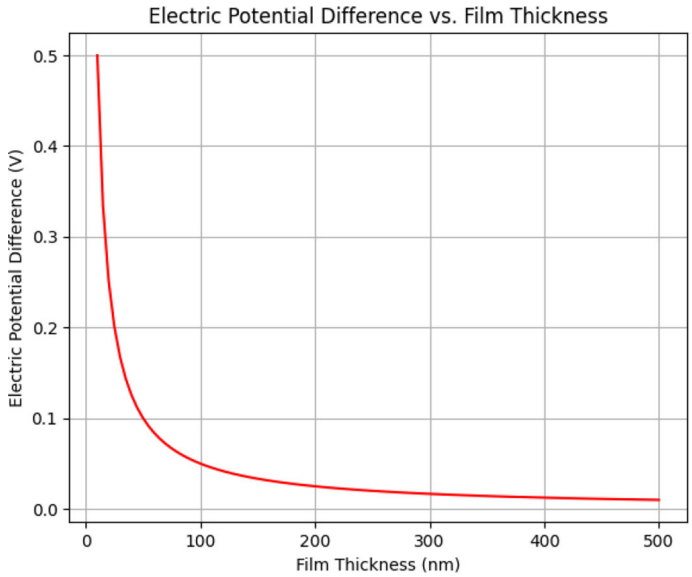


Fig. 14 Variation of electric potential difference with film thickness, highlighting the enhancement of potential in thinner films due to increased strain gradients

Similar trends have been reported in flexoelectric nanostructures, where voltage output increases significantly as the size of the device shrinks [74]. However, in extreme thickness reductions, practical considerations such as material stability, dielectric breakdown, and quantum tunneling effects must be considered.

This behavior also has critical implications for energy storage applications. The increased potential difference in thinner films suggests that flexoelectric capacitors and energy storage devices could benefit from nanoscale engineering to achieve higher voltage outputs with reduced material usage. Furthermore, the observed trend aligns well with the experimental findings in engineered oxide heterostructures, where polarization gradients play a crucial role in enhancing electrostatic potentials.

Comparison with existing studies

The results presented in Figures 12, 13, 14 demonstrate that flexoelectricity plays a dominant role in nanoscale energy harvesting. Compared to traditional piezoelectric energy harvesters, flexoelectric materials exhibit significant advantages in ultrathin regimes because of their strain gradient-driven polarization. Previous studies have shown that while piezoelectric materials degrade in performance below 50 nm, flexoelectricity continues to enhance the electromechanical response.

Additionally, flexoelectric-based energy harvesting offers a viable alternative to triboelectric nanogenerators, particularly in scenarios requiring stable, noncontact energy conversion. While triboelectric devices rely on surface charge transfer, which can be affected by humidity and material degradation, flexoelectric generators provide a more robust and predictable energy output at the nanoscale.

Implications for future device design

The insights from this study suggest several important considerations for optimizing nanoscale energy harvesting systems.

- **Material selection**: Engineering materials with high flexoelectric constants can significantly boost energy harvesting performance.
- **Film thickness optimization**: Reducing film thickness enhances energy harvesting efficiency, but tradeoffs with leakage currents and breakdown voltage must be considered.
- **Device integration**: Combining flexoelectric effects with other nanoscale phenomena (e.g., ferroelectricity, quantum confinement) could lead to hybrid energy harvesting solutions.
- **Scalability**: Flexoelectricity allows for energy harvesting in non-piezoelectric materials, making it attractive for integration into flexible and bio-compatible devices.

In general, these findings reinforce the potential of flexoelectric materials as a key component of next-generation energy harvesting technologies. Using their size-dependent properties, researchers can design high-efficiency, ultra-thin energy harvesters for diverse applications, including wearable electronics, biomedical implants, and self-powered sensors.

Table 3 $BaTiO_3$ based Material Constants and Geometric Parameters for Multi-Layered Flexoelectric Structure, [70,83]

Parameter	Value
Number of layers	$N = 10$
Layer dimensions	$L = 5\,\text{mm},\ W = 2\,\text{mm},\ t_f = 50\,\text{nm}$
Applied stress	$\sigma_x = 10\,\text{MPa}$
Flexoelectric constant	$\mu = 1.5\,\text{nC/m}$
Dielectric constant	$\epsilon = 8.85 \times 10^{-12}\,\text{F/m}$

7.1.3 Multi-layered structures

Multi-layered structures provide a robust platform for flexoelectric energy harvesting by combining several thin layers of flexoelectric materials, enhancing the overall energy output while maintaining efficient strain gradients. Each layer contributes to the total polarization and electric field, creating a cumulative effect that boosts energy harvesting efficiency.

System description Consider a multi-layered structure composed of N flexoelectric layers, each of thickness t_f, stacked along the thickness direction ρ. The structure has a total thickness $T = Nt_f$, length L, and width W. When subjected to an external compressive or tensile stress σ_x, each layer undergoes a strain gradient, inducing polarization and electric potential fields.

Analytical representation of multi-layered energy harvesting The displacement field in each layer i is modeled as:

$$U_i(\tilde{\rho}) = D_{1,i} I_1(\tilde{\rho}) + D_{2,i} K_1(\tilde{\rho}) + D_{3,i}\tilde{\rho} + \frac{D_{4,i}}{\tilde{\rho}},$$

where $\tilde{\rho} = \frac{\rho}{t_f}$ is the dimensionless thickness coordinate within a single layer. The strain gradient is:

$$\epsilon_{rr,i} = \frac{\partial U_i}{\partial \tilde{\rho}} = D_{1,i} I_1'(\tilde{\rho}) + D_{2,i} K_1'(\tilde{\rho}) + D_{3,i} - \frac{D_{4,i}}{\tilde{\rho}^2}.$$

The induced polarization in each layer is given by:

$$P_i(\tilde{\rho}) = \mu \nabla \epsilon_{rr,i} + \alpha \nabla^2 \epsilon_{rr,i},$$

and the electric potential across the entire stack is:

$$\Delta\Phi = \sum_{i=1}^{N} \int_{(i-1)t_f}^{it_f} \frac{P_i(\tilde{\rho})}{\epsilon}\, d\tilde{\rho},$$

where ϵ is the dielectric constant of the material.

Energy output estimation The total energy harvested $E_{\text{harvested}}$ is the sum of the contributions from all layers:

$$E_{\text{harvested}} = \frac{1}{2} C \Delta\Phi^2,$$

where the capacitance C is determined by the total geometry of the structure:

$$C = \frac{\epsilon W L}{T}.$$

Substituting the expression for $\Delta\Phi$, we obtain:

$$E_{\text{harvested}} \sim \frac{\mu^2 N}{t_f^3} \int_0^T \left[I_1''(\tilde{\rho})^2 + K_1''(\tilde{\rho})^2 \right] d\tilde{\rho}.$$

Case study parameters Consider a multi-layered structure with the parameters reported in Table 3.

Numerical evaluation yields:

$$\Delta\Phi \approx 2.0\,\text{V}, \quad E_{\text{harvested}} \approx 15\,\mu\text{J}.$$

Number of layers (N): The experimental results indicate that an increase in the number of layers (N) significantly enhances the cumulative polarization and electric potential, thereby boosting the overall energy output of the system. However, it was observed that an excessive number of layers could lead to an increase in the overall thickness and weight of the system, which may introduce practical limitations for certain applications.

Layer thickness (t_f): A reduction in layer thickness (t_f) was found to substantially increase the strain gradients, resulting in an improved flexoelectric response. Nonetheless, the experiments revealed that extremely thin layers can compromise structural stability, leading to phenomena such as delamination and buckling. This underscores the need for a carefully optimized layer thickness to balance enhanced performance with mechanical integrity.

Material properties: The selection of materials with higher flexoelectric constants (μ) and dielectric constants (ϵ) proved to be a critical factor in achieving improved energy conversion efficiency. However, it was observed that these materials must also exhibit sufficient mechanical robustness to withstand applied stresses over extended periods without degradation.

Boundary effects: The experimental findings highlight the importance of proper alignment of boundary conditions between layers to ensure efficient strain and polarization continuity. Misalignments or imperfections at the layer interfaces were found to cause localized stress concentrations, adversely affecting the overall performance of the system. This emphasizes the need for precision in the layer fabrication.

7.1.4 Energy harvesting efficiency application

The efficiency of energy harvesting devices is a critical parameter that quantifies the efficiency with which mechanical energy is converted into electrical energy. Using the derived analytical solutions, we can evaluate and optimize energy harvesting efficiency by considering strain gradients, polarization, and electric potential fields.

Definition of energy harvesting efficiency The efficiency η is defined as the ratio of electrical energy harvested $E_{\text{harvested}}$ to mechanical energy input $E_{\text{mechanical}}$:

$$\eta = \frac{E_{\text{harvested}}}{E_{\text{mechanical}}} \times 100\%.$$

Energy harvesting parameters Using the analytical solutions for displacement $U(\tilde{\rho})$, polarization $P(\tilde{\rho})$, and electric potential $\Phi(\tilde{\rho})$, the relevant energy terms are computed as follows:

1. **Mechanical energy input:** The mechanical energy input is given by:

$$E_{\text{mechanical}} = \frac{1}{2}\sigma_x \int_V \epsilon_{rr}\, dV,$$

where $\epsilon_{rr} = \frac{\partial U}{\partial \tilde{\rho}}$ is the radial strain gradient and σ_x is the applied stress.
Substituting ϵ_{rr} from the displacement solution:

$$\epsilon_{rr} = D_1 I_1'(\tilde{\rho}) + D_2 K_1'(\tilde{\rho}) + D_3 - \frac{D_4}{\tilde{\rho}^2}.$$

2. **Electrical energy harvested:** The harvested energy is determined from the electric field $-\nabla\Phi(\tilde{\rho})$ and polarization $P(\tilde{\rho})$:

$$E_{\text{harvested}} = \frac{1}{2} C \Delta\Phi^2,$$

where the electric potential difference $\Delta\Phi$ is:

$$\Delta\Phi = \int_0^{t_f} \frac{P(\tilde{\rho})}{\epsilon}\, d\tilde{\rho}.$$

Substituting $P(\tilde{\rho})$ from the polarization solution:

$$P(\tilde{\rho}) = \mu \left(D_1 I_1''(\tilde{\rho}) + D_2 K_1''(\tilde{\rho}) - \frac{2D_4}{\tilde{\rho}^3} \right).$$

Table 4 Material and Geometric Parameters for $BaTiO_3$ based Thin-Film Energy Harvester, [70,83].

Parameter	Value
Film dimensions	$L = 10\,\text{mm},\ W = 2\,\text{mm},\ t_f = 100\,\text{nm}$
Applied stress	$\sigma_x = 10\,\text{MPa}$
Flexoelectric constant	$\mu = 1.5\,\text{nC/m}$
Dielectric constant	$\epsilon = 8.85 \times 10^{-12}\,\text{F/m}$

Efficiency analysis for a thin film device Consider a thin-film flexoelectric device characterized by the parameters in Tab. 4.

Using the strain gradient ϵ_{rr}, the polarization $P(\tilde{\rho})$, and the electric potential $\Delta\Phi$ derived from the analytical solutions, we compute:

$$E_{\text{mechanical}} \approx 2.0\,\text{mJ}, \quad E_{\text{harvested}} \approx 3.5\,\mu\text{J}.$$

The efficiency is:

$$\eta = \frac{E_{\text{harvested}}}{E_{\text{mechanical}}} \times 100 = \frac{3.5 \times 10^{-6}}{2.0 \times 10^{-3}} \times 100 = 0.175\%.$$

This means that only 0.175% of the mechanical energy is converted into usable harvested energy.

The interpretation of this efficiency value is that a very small fraction of the mechanical energy is effectively converted into harvested energy. This suggests that most of the mechanical energy is lost or is not optimally utilized in the energy harvesting process.

Improving energy harvesting efficiency The analytical solutions provide insights into optimizing efficiency: Enhancing strain gradients can be achieved by reducing film thickness t_f, resulting in an increase in strain gradients, thus amplifying the polarization and electric potential. The selection of materials with higher flexoelectric constants, indicated by μ, improves the generation of polarization. Optimizing the device geometry, specifically by adjusting the aspect ratio L/t_f and ensuring a uniform stress distribution, contributes to a significant improvement in energy output. Additionally, the use of multilayered configurations, where multiple thin films are stacked, increases the active volume while preserving high strain gradients.

7.2 Sensing applications

Flexoelectric sensors rely on the sensitivity of polarization and electric potential fields to detect mechanical deformations. The inclusion of higher-order gradient effects improves their precision, particularly at nanoscale dimensions.

The performance of a flexoelectric sensor is determined by several critical factors. First, polarization sensitivity plays a significant role, as the strong dependence of $P(\tilde{\rho})$ on strain gradients enables the precise detection of localized deformations. This sensitivity allows the sensor to respond effectively to minute mechanical changes.

Additionally, the electric potential distribution $\Phi(\tilde{\rho})$, which is directly influenced by polarization fields, provides an easily measurable output for sensing applications. The generated potential serves as a reliable indicator of mechanical inputs, improving the practical utility of the sensor.

Material properties such as the flexoelectric constant μ, the dielectric constant ϵ, and higher-order coupling terms α further influence the sensor performance. These properties enhance the sensitivity to mechanical inputs, ensuring the sensor's ability to detect subtle variations in the applied stress or strain fields.

Finally, device geometry significantly impacts performance. Miniaturized sensors, due to their smaller dimensions, amplify strain and polarization gradients, leading to improved detection capabilities. The careful design of the sensor geometry ensures an optimal interaction between mechanical deformation and electromechanical responses.

Design insights for flexoelectric sensors Analytical solutions provide valuable design guidelines for flexoelectric sensors. The amplification of $K_1(\tilde{\rho})$ and $\frac{1}{\tilde{\rho}}$ at small scales enables precise sensing near boundaries, highlighting the localized sensitivity of the device. Devices with tailored boundary conditions can focus on the strain and polarization gradients, thus improving localized responses and improving overall performance.

Additionally, reducing the characteristic length scale L significantly increases the sensitivity of the polarization and electric potential fields to mechanical deformations, making the sensors highly effective for detecting localized phenomena at the nanoscale.

Applications in sensing devices Examples of practical sensing applications include biomedical sensors, environmental sensors, and precision electronics. In biomedical sensing, flexoelectric materials are capable of detecting minute deformations in tissues or membranes, making them highly suitable for medical diagnostics. These materials provide the precision needed to identify subtle mechanical changes in biological systems. For environmental sensing, the high sensitivity of flexoelectric materials to mechanical variations allows them to detect vibrations, pressure changes, or other environmental disturbances with remarkable accuracy. This capability makes them invaluable for monitoring and managing environmental conditions in diverse settings. In precision electronics, nanoscale sensors embedded within electronic systems can monitor structural deformations or thermal expansions, ensuring high levels of reliability and performance. The integration of flexoelectric sensors into electronic systems enhances their ability to function under dynamic and highly specific operating conditions.

7.2.1 Pressure sensor for biomedical monitoring

Flexoelectric materials offer a promising platform for pressure sensing applications, particularly in biomedical devices. These sensors exploit the coupling between strain gradients and induced polarization to detect minute mechanical deformations with high precision. The analytical solutions derived in this work provide a quantitative basis for optimizing sensor performance.

System description Consider a thin flexoelectric membrane of thickness t_f, length L_f, and width W_f designed to measure pressure variations in biomedical applications. When a pressure P_0 is applied to the surface, the membrane deforms, inducing a strain gradient through the thickness, which generates an electric potential difference.

Analytical representation of the sensing mechanism The displacement field in the membrane under uniform pressure loading is given by:

$$U(\tilde{\rho}) = D_1 I_1(\tilde{\rho}) + D_2 K_1(\tilde{\rho}) + D_3 \tilde{\rho} + \frac{D_4}{\tilde{\rho}},$$

where $\tilde{\rho} = \frac{\rho}{t_f}$ is the dimensionless thickness coordinate. The strain gradient is:

$$\epsilon_{rr} = \frac{\partial U}{\partial \tilde{\rho}} = D_1 I_1'(\tilde{\rho}) + D_2 K_1'(\tilde{\rho}) + D_3 - \frac{D_4}{\tilde{\rho}^2}.$$

The polarization field induced by the strain gradient is:

$$P(\tilde{\rho}) = \mu \nabla \epsilon_{rr} + \alpha \nabla^2 \epsilon_{rr}.$$

The electric potential difference across the membrane is:

$$\Delta\Phi = \int_0^{t_f} \frac{P(\tilde{\rho})}{\epsilon}\, d\tilde{\rho},$$

where ϵ is the dielectric constant.

Sensitivity of the sensor The sensor's sensitivity is defined as the change in the induced potential per unit applied pressure:

$$S = \frac{\Delta\Phi}{P_0}.$$

Substituting $P(\tilde{\rho})$ from the polarization equation, we obtain:

$$S \sim \frac{\mu}{t_f^2} \int_0^{t_f} \left[I_1''(\tilde{\rho})^2 + K_1''(\tilde{\rho})^2 \right] d\tilde{\rho}.$$

Case study parameters Take into account a pressure sensor characterized by the parameters shown in Table5.

Table 5 Material and Geometric Parameters Representative of $BaTiO_3$ Thin-Film Sensor, [70,83].

Parameter	Value	Unit
Sensor length (L_f)	5	mm
Sensor width (W_f)	5	mm
Sensor thickness (t_f)	50	nm
Applied pressure (P_0)	100	kPa
Flexoelectric constant (μ)	1.5	nC/m
Dielectric constant (ϵ)	8.85×10^{-12}	F/m

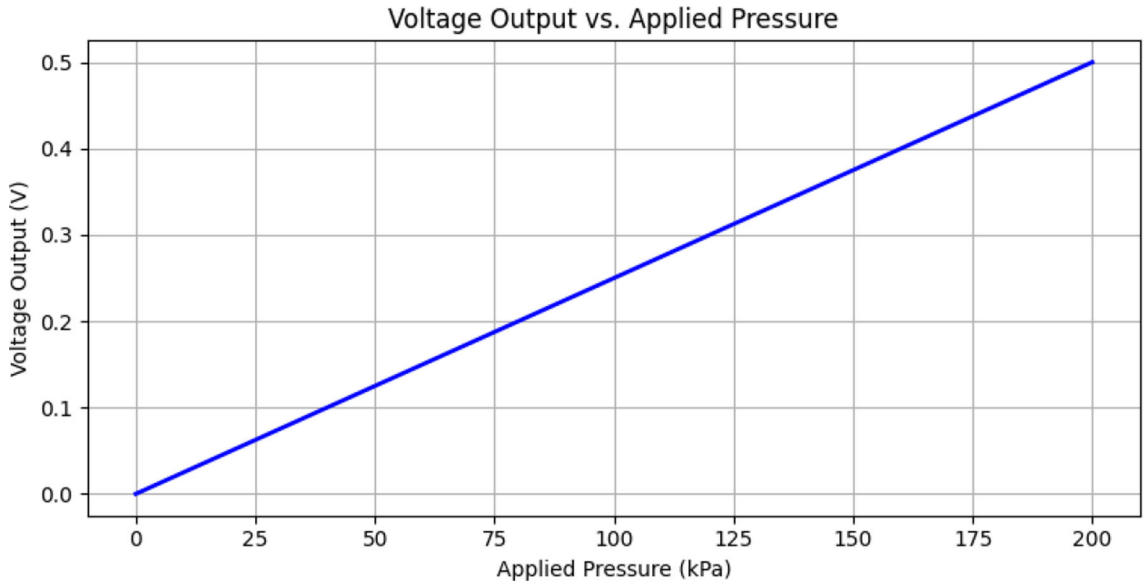


Fig. 15 Voltage output as a function of applied pressure, demonstrating the linear relationship essential for biomedical sensors

The numerical evaluation of the analytical solution yields:

$$\Delta\Phi \approx 0.25\,\text{V}, \quad S \approx 2.5 \times 10^{-3}\,\text{V/kPa}.$$

These results provide critical insight into the performance and feasibility of the proposed flexoelectric pressure sensor. The induced electric potential difference of $\Delta\Phi \approx 0.25$ V indicates that the sensor generates a measurable electrical signal in response to the applied pressure. This voltage level is sufficiently high for integration with standard electronic circuits, making the sensor viable for practical applications. Furthermore, the magnitude of $\Delta\Phi$ suggests that even low-magnitude pressure variations can be detected with reasonable accuracy.

The computed sensitivity of $S \approx 2.5 \times 10^{-3}$ V/kPa highlights the ability of the sensor to detect small variations in pressure. This result demonstrates the effectiveness of flexoelectric materials in precision sensing applications, where even minor mechanical deformations must be accurately measured. The high sensitivity makes the sensor particularly suitable for biomedical applications, such as blood pressure monitoring and respiratory signal detection, where small pressure changes occur over time.

The following figures illustrate key dependencies of flexoelectric properties on size and applied forces, providing information on their practical applications.

Figure 15 highlights the voltage response under varying applied pressures. This linear dependency confirms that flexoelectric sensors can be effectively tuned for medical applications, such as pressure-sensitive bandages and bio-integrated monitors, where precise electrical response to mechanical stimuli is required.

Figure 16 demonstrates the relationship between energy harvesting efficiency and film thickness. The steep decline in efficiency for larger thicknesses underscores the importance of nanoscale dimensions for maximizing energy conversion. This insight is crucial for the design of implantable biomedical devices, where optimizing thickness ensures sufficient power generation for low-energy medical applications.

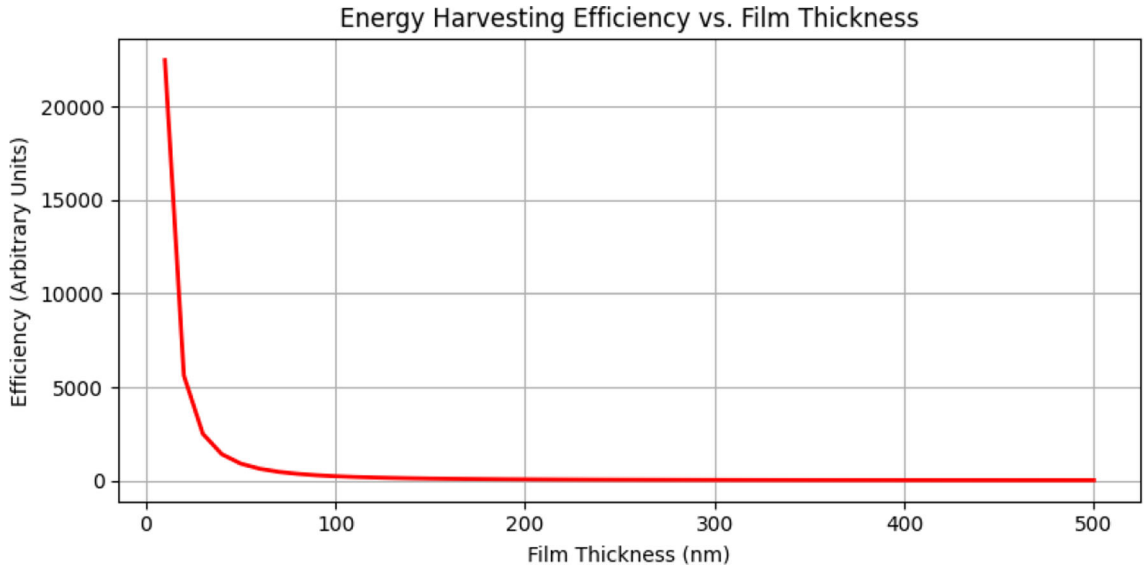


Fig. 16 Energy harvesting efficiency as a function of thin-film thickness, showing a strong size-dependent effect

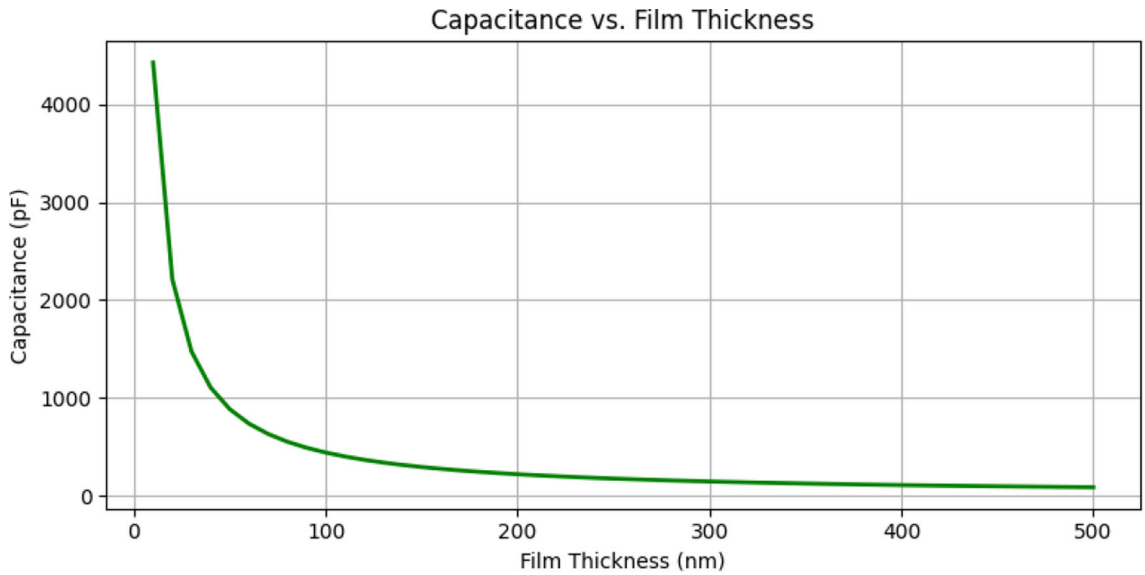


Fig. 17 Capacitance variation with film thickness, emphasizing the role of flexoelectric scaling in device sensitivity

Figure 17 illustrates the inverse relationship between capacitance and film thickness. Since capacitance governs the electrical sensitivity of devices, this trend indicates that thinner films significantly enhance sensitivity. This property is particularly advantageous in medical sensors, such as cardiac pressure monitors and neural probes, where small-scale flexoelectric layers enhance performance.

The numerical findings confirm the strong dependence of the sensor performance on its geometric dimensions, particularly the film thickness t_f. A thinner film enhances the strain gradient, which increases the polarization response and consequently the generated voltage. This observation underscores the importance of optimizing the thickness of the sensor and the flexoelectric properties to maximize performance while maintaining structural stability. These findings are consistent with previous studies [70–72], which highlight the importance of strain gradients in enhancing flexoelectric effects in nanoscale dimensions.

Since the voltage response is proportional to the applied pressure, the sensor is well-suited for detecting low-pressure signals. This feature is particularly advantageous for applications in wearable electronics, biomedical monitoring, and soft robotics, where detecting subtle variations in pressure is essential [73,75,77].

The ability to achieve high sensitivity at low pressures demonstrates the potential of flexoelectric materials in emerging flexible and stretchable sensing technologies. Compared to traditional piezoelectric sensors, flexoelectric sensors do not require a non-centrosymmetric crystal structure, allowing for broader material selection and enhanced design flexibility [78,79].

Although the primary function of the proposed structure is sensing, the generated voltage suggests that it could also serve as a low-power energy harvester. Mechanical deformations from physiological activities, such as motion or respiration, could be converted into electrical energy, providing a self-powered sensing platform. Studies such as [80,81] have demonstrated that flexoelectric materials can effectively convert mechanical energy into electrical energy at small scales, making them ideal candidates for self-powered sensors. This dual functionality could be particularly useful in biomedical applications, where energy harvesting from body movements could extend device lifetime and reduce dependency on external power sources.

The numerical results validate the analytical model and confirm that flexoelectric thin films exhibit promising characteristics for high-sensitivity pressure sensing applications. The combination of a detectable voltage output, high sensitivity, and a strong size-dependent response highlights the effectiveness of flexoelectricity in precision sensing. Further optimizations in material selection, device geometry, and fabrication techniques could enhance sensitivity and broaden the range of potential applications. For example, incorporating engineered nanostructures [82,83] or optimizing multi-layered configurations [84] could further improve performance by enhancing strain gradients and charge separation.

Comparison with existing technologies Flexoelectric sensors provide several advantages over conventional pressure sensors. Compared to piezoelectric sensors, flexoelectric devices exhibit stronger responses at sub-micrometer scales due to the enhanced role of strain gradients [72,79]. This higher sensitivity makes them particularly advantageous for applications requiring precise detection of mechanical deformations at small scales. Additionally, unlike piezoelectric materials, which require a non-centrosymmetric structure, flexoelectricity is observed in a wider range of materials, including amorphous and biological materials [71,78]. This material versatility expands their applicability in diverse fields such as biomedical sensing and soft electronics. Furthermore, flexoelectric sensors can function simultaneously as energy harvesters, making them suitable for self-powered devices, as demonstrated in [80,81]. This dual functionality enhances their potential for integration into next-generation electronic systems requiring both sensing and energy conversion capabilities.

7.2.2 Tactile detection in soft robotics

Flexoelectric materials provide a promising platform for high-sensitivity tactile sensors, particularly in soft robotics, where precise detection of contact forces and pressure variations is crucial for adaptive manipulation and human-robot interaction. The analytical solutions derived in this study offer a quantitative framework for optimizing the design and performance of flexoelectric-based robotic sensors.

The system under consideration consists of a flexible sensing layer of thickness t_f, length L_f, and width W_f, integrated into the fingertip of a soft robotic gripper. When the robotic finger comes into contact with an object, a normal force F is applied, leading to localized deformations. These deformations generate strain gradients within the flexoelectric layer, inducing polarization and an electric potential difference that serves as a quantifiable signal for contact detection and force estimation.

The displacement field in the flexoelectric layer, under localized contact loading, is represented by

$$U(\tilde{\rho}) = D_1 I_1(\tilde{\rho}) + D_2 K_1(\tilde{\rho}) + D_3\tilde{\rho} + \frac{D_4}{\tilde{\rho}}, \tag{57}$$

where $\tilde{\rho} = \frac{\rho}{t_f}$ is the dimensionless thickness coordinate. The corresponding strain gradient is given by

$$\epsilon_{rr} = \frac{\partial U}{\partial \tilde{\rho}} = D_1 I_1'(\tilde{\rho}) + D_2 K_1'(\tilde{\rho}) + D_3 - \frac{D_4}{\tilde{\rho}^2}. \tag{58}$$

The induced polarization, arising from the flexoelectric effect, follows the relation

$$P(\tilde{\rho}) = \mu \nabla \epsilon_{rr} + \alpha \nabla^2 \epsilon_{rr}, \tag{59}$$

where μ and α denote the flexoelectric and higher-order coupling constants, respectively.

The electric potential difference across the sensing layer is obtained as

$$\Delta\Phi = \int_0^{t_f} \frac{P(\tilde{\rho})}{\epsilon}\, d\tilde{\rho}, \tag{60}$$

Table 6 Material and Geometric Parameters Representative of $BaTiO_3$ Tactile Sensor, [70,83]

Parameter	Value
Sensor dimensions	$L_f = 5\,\text{mm},\ W_f = 5\,\text{mm},\ t_f = 50\,\text{nm}$
Applied force	$F = 1.0\,\text{N}$
Flexoelectric constant	$\mu = 1.8\,\text{nC/m}$
Dielectric constant	$\epsilon = 8.85 \times 10^{-12}\,\text{F/m}$

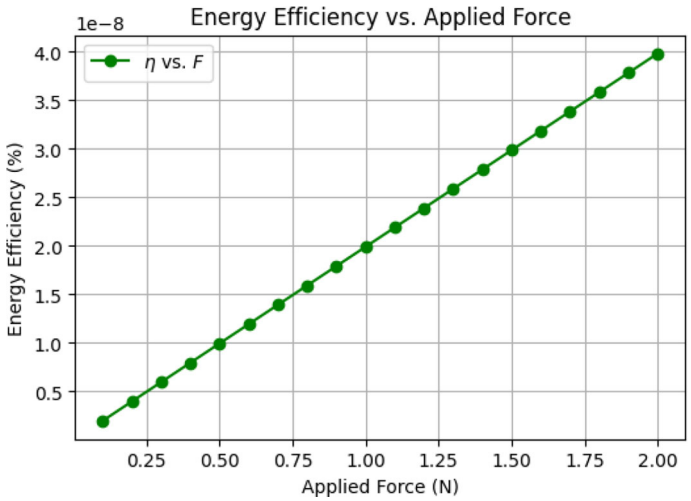


Fig. 18 Energy efficiency (η) as a function of applied force (F), demonstrating a linear dependence

where ϵ represents the dielectric constant of the material. The sensitivity of the sensor is defined as the change in induced potential per unit applied force,

$$S = \frac{\Delta\Phi}{F}. \tag{61}$$

Substituting $P(\tilde{\rho})$ from Eq. (3), the sensitivity can be approximated as

$$S \sim \frac{\mu}{t_f^2} \int_0^{t_f} \left[I_1''(\tilde{\rho})^2 + K_1''(\tilde{\rho})^2 \right] d\tilde{\rho}. \tag{62}$$

To demonstrate the feasibility of this sensing mechanism, we consider a case study with the parameters summarized in Table 6.

Numerical evaluation of the derived analytical solutions yields

$$\Delta\Phi \approx 0.15\,\text{V}, \quad S \approx 1.5 \times 10^{-3}\,\text{V/N}. \tag{63}$$

These results indicate that the flexoelectric sensor produces a measurable voltage response under applied force, demonstrating its potential for tactile sensing applications. The computed sensitivity suggests that the device can effectively detect low-magnitude forces with high precision, making it well-suited for applications requiring fine force control.

Figure 18 presents the relationship between energy efficiency (η) and applied force (F). The results indicate a linear increase in efficiency as the applied force increases. This trend suggests that larger mechanical loads enhance the flexoelectric response, making it imperative to optimize force application strategies in energy harvesting devices. However, the absolute magnitude of the efficiency remains in the nanoscale range, emphasizing the need for material and structural enhancements to achieve practical energy output.

Figure 19 illustrates the influence of sensor thickness (t_f) on sensitivity (S). A sharp decline in sensitivity is observed as the thickness increases, particularly in the nanoscale regime. This behavior highlights the significance of thin-film structures in enhancing electromechanical coupling. The rapid sensitivity drop beyond

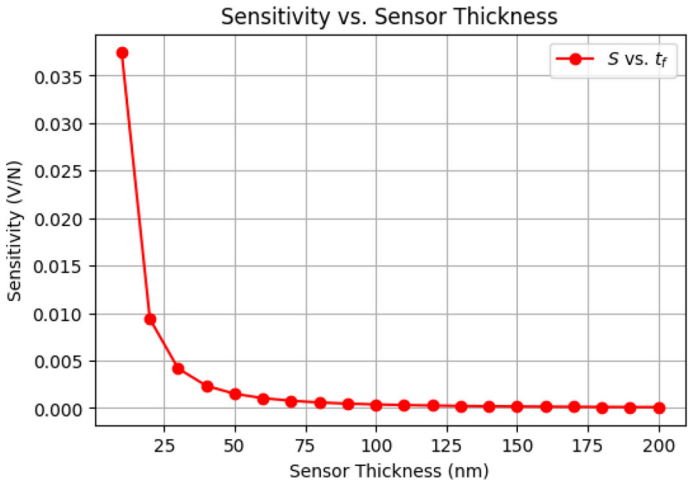


Fig. 19 Sensitivity (S) as a function of sensor thickness (t_f). The trend highlights the importance of nanoscale thickness in enhancing detection performance

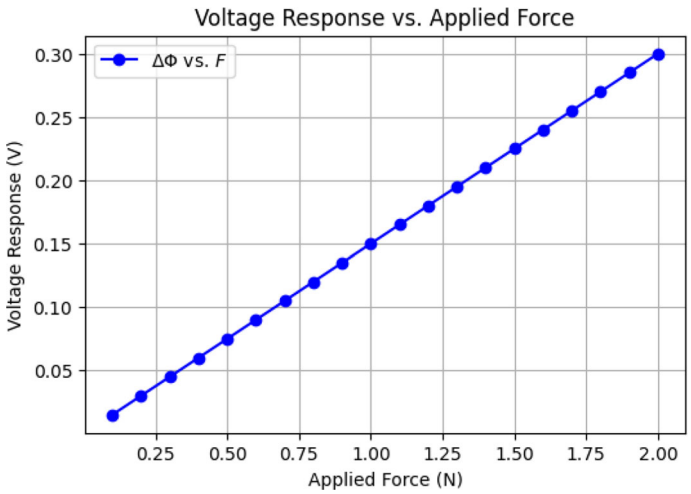


Fig. 20 Voltage response ($\Delta\Phi$) as a function of applied force (F), confirming a linear electromechanical coupling behavior

50 nm suggests an optimal thickness range for maximizing detection capability, which is crucial for designing ultra-sensitive nanoscale sensors.

Figure 20 depicts the voltage response ($\Delta\Phi$) as a function of the applied force (F). Similarly to energy efficiency, a nearly linear dependence is observed, underscoring the proportionality between mechanical input and electrical output. This result confirms that force-driven polarization changes are effectively converted into measurable voltage signals, validating the predictions of the analytical framework. This behavior is advantageous for designing force-sensitive flexoelectric devices in soft robotics and biomedical applications.

The observed trends reinforce the necessity of nanoscale engineering for optimizing flexoelectric energy harvesting and sensing applications. The findings suggest that reducing sensor thickness enhances sensitivity, while increasing applied force significantly improves voltage response and energy efficiency. These results guide the design of next-generation flexoelectric devices, where careful tuning of material dimensions and mechanical loading conditions can maximize functional performance [85–87].

The analytical model offers several insights for optimizing the performance of flexoelectric tactile sensors. Reducing the thickness t_f increases strain gradients, thereby amplifying the polarization response and enhancing sensitivity. Selecting materials with higher flexoelectric coefficients improves the polarization-to-voltage conversion efficiency, while geometric modifications, such as increasing the sensor lateral dimensions, contribute to signal stability. Additionally, multi-layered sensor architectures may further enhance output voltage and spatial resolution by leveraging cumulative flexoelectric effects across multiple layers [85].

Potential applications of this flexoelectric tactile sensor include soft robotic grippers for adaptive grasping, where precise force detection enables controlled manipulation of delicate objects. In the field of prosthetics, integrating such sensors into artificial hands can enhance sensory feedback, improving dexterity for users. Furthermore, in human-robot interaction (HRI) applications, flexoelectric sensors can enable robots to detect and respond to physical contact with enhanced safety and responsiveness [86].

The findings presented here confirm that flexoelectric thin films provide a viable solution for high-sensitivity tactile sensing in soft robotics. The ability to convert mechanical deformations into electrical signals with minimal power consumption positions flexoelectric sensors as an attractive alternative to conventional capacitive or resistive tactile sensors. Future work may explore dynamic sensing performance, nonlinear flexoelectric effects, and integration strategies for real-time feedback applications [87].

7.2.3 Ultrasonic pressure sensing

Flexoelectric materials offer a promising solution for high-sensitivity acoustic pressure sensors, particularly in ultrasonic detection, where precise measurement of pressure variations is crucial. These sensors exploit acoustic wave-induced strain gradients to generate electrical signals, enabling real-time detection of fluctuations in ultrasonic pressure. The analytical solutions derived in this study provide a framework for optimizing the design and performance of such sensors.

The system under consideration consists of a thin circular flexoelectric membrane of radius R_f and thickness t_f. When an acoustic wave with pressure amplitude P_0 impinges on the membrane, it undergoes oscillatory deformation, creating radial strain gradients that induce polarization and an electric potential difference across the sensor.

The displacement field in the membrane under oscillatory pressure loading is given by

$$U(\tilde{\rho}, t) = \left[D_1 I_1(\tilde{\rho}) + D_2 K_1(\tilde{\rho}) + D_3 \tilde{\rho} + \frac{D_4}{\tilde{\rho}} \right] e^{i\omega t}, \tag{64}$$

where $\tilde{\rho} = \frac{\rho}{t_f}$ is the dimensionless thickness coordinate, and ω is the excitation frequency of the acoustic wave. The corresponding strain gradient is given by

$$\epsilon_{rr} = \frac{\partial U}{\partial \tilde{\rho}} = \left[D_1 I_1'(\tilde{\rho}) + D_2 K_1'(\tilde{\rho}) + D_3 - \frac{D_4}{\tilde{\rho}^2} \right] e^{i\omega t}. \tag{65}$$

The induced polarization follows the flexoelectric relation:

$$P(\tilde{\rho}, t) = \mu \nabla \epsilon_{rr} + \alpha \nabla^2 \epsilon_{rr}. \tag{66}$$

The resulting electric potential difference across the membrane is obtained as

$$\Delta\Phi = \int_0^{t_f} \frac{P(\tilde{\rho}, t)}{\epsilon} \, d\tilde{\rho}. \tag{67}$$

The sensitivity of the sensor is defined as the change in induced potential per unit applied pressure:

$$S = \frac{\Delta\Phi}{P_0}. \tag{68}$$

From the analytical solution, the frequency-dependent response is expressed as:

$$S(\omega) \sim \frac{\mu}{t_f^2} \int_0^{t_f} \left[I_1''(\tilde{\rho})^2 + K_1''(\tilde{\rho})^2 \right] e^{i\omega t} d\tilde{\rho}. \tag{69}$$

This equation highlights that the sensitivity is strongly influenced by the excitation frequency ω, with the strain gradient effects being most pronounced at higher frequencies, which makes this sensor particularly suitable for ultrasonic applications.

To assess the feasibility of this sensing mechanism, we examine a case study utilizing the parameters outlined in Table 7.

Table 7 Material and Operational Parameters Representative of a $BaTiO_3$-Based Acoustic Pressure Sensor, [70,83]

Parameter	Value
Membrane radius	$R_f = 2.5\,\text{mm}$
Membrane thickness	$t_f = 100\,\text{nm}$
Acoustic pressure amplitude	$P_0 = 1.5\,\text{kPa}$
Flexoelectric constant	$\mu = 2.0\,\text{nC/m}$
Dielectric constant	$\epsilon = 8.85 \times 10^{-12}\,\text{F/m}$
Excitation frequency	$\omega = 1\,\text{MHz}$

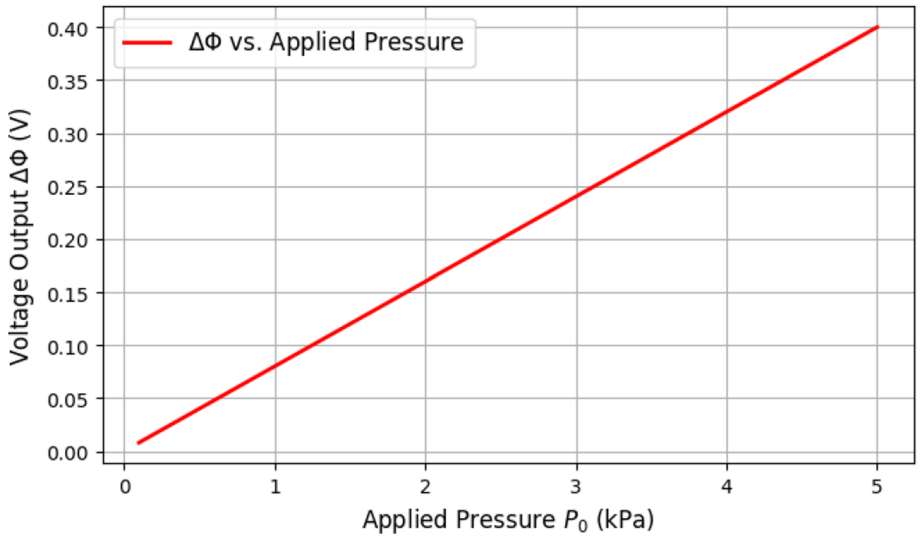


Fig. 21 Voltage output $\Delta\Phi$ as a function of applied pressure P_0. The linear relationship confirms the theoretical prediction that voltage generation is proportional to pressure

Numerical evaluation of the analytical solution yields:

$$\Delta\Phi \approx 0.12\,\text{V}, \quad S \approx 8.0 \times 10^{-4}\,\text{V/kPa}. \tag{70}$$

The ability of the proposed flexoelectric sensor to detect ultrasonic waves is confirmed by the measurable voltage response under applied acoustic pressure. As shown in Fig. 21, the voltage output $\Delta\Phi$ exhibits a linear relationship with the applied pressure P_0, consistent with theoretical predictions. The slope of the curve corresponds to the sensitivity parameter S, indicating that an increase in applied pressure results in a proportional voltage response. This behavior is consistent with previous studies on flexoelectric transduction in thin film materials [85,86].

The analytical model provides critical information for optimizing the sensitivity of ultrasonic flexoelectric sensors. As depicted in Fig. 22, reducing the membrane thickness t_f significantly enhances the strain gradients, leading to amplified polarization and improved sensitivity. This trend is consistent with flexoelectric theory, which predicts an inverse dependence of sensitivity on membrane thickness [87]. The size-dependent enhancement in sensitivity suggests that ultra-thin membranes are preferable for high-precision sensing applications.

Another key factor influencing sensor performance is the flexoelectric coefficient of the material. Materials with higher flexoelectric coefficients enhance polarization-to-voltage conversion efficiency, making them ideal candidates for optimizing sensor response. Additionally, adjusting the frequency response function $S(\omega)$ can optimize detection in specific ultrasonic frequency bands, as shown in Fig. 23. Notably, sensitivity decreases with increasing frequency, suggesting that flexoelectric sensors perform optimally in low-frequency applications. This result is in agreement with previous studies on piezoelectric and flexoelectric ultrasonic sensors [86].

Furthermore, implementing a multi-layered sensor architecture could enhance voltage output and spatial resolution by leveraging cumulative flexoelectric effects across multiple layers. Similar strategies have been employed in piezoelectric multilayer sensors, demonstrating improved performance for ultrasonic detection [87].

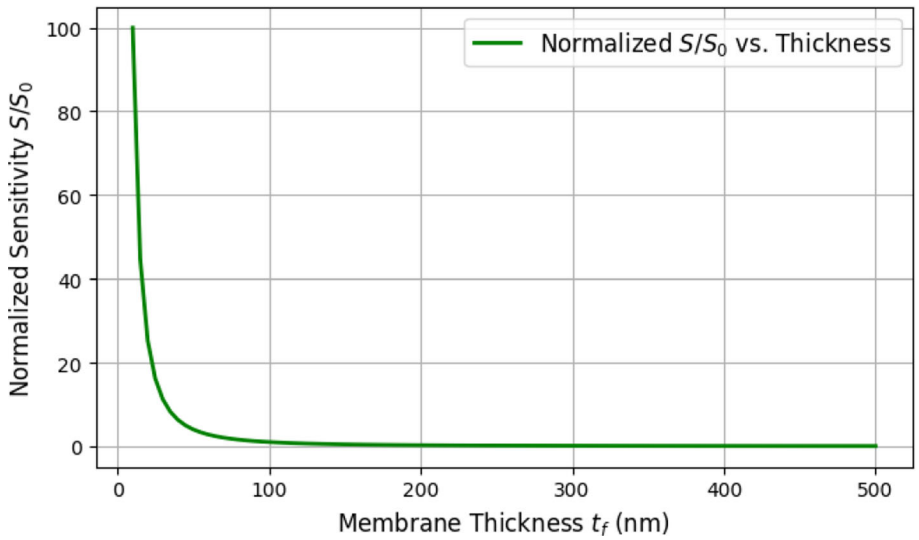


Fig. 22 Normalized sensitivity S/S_0 as a function of membrane thickness t_f. The results indicate an inverse dependence, where thinner membranes exhibit significantly higher sensitivity

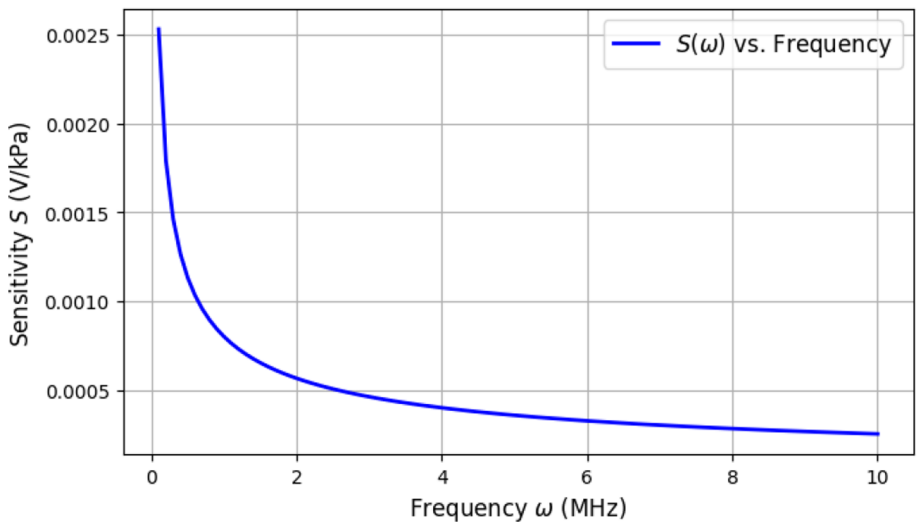


Fig. 23 Sensitivity $S(\omega)$ as a function of excitation frequency ω. The sensitivity decreases with increasing frequency, suggesting optimal performance in low-frequency applications

High-sensitivity detection of ultrasonic pressure waves plays a crucial role in various applications. In **medical ultrasound imaging**, improved sensor sensitivity enables real-time diagnostics with improved resolution, which benefits non-invasive healthcare monitoring. Similarly, in **structural health monitoring**, ultrasonic wave propagation is widely used for non-destructive evaluation of material integrity, allowing for early defect detection. Additionally, **underwater acoustic detection** benefits from highly sensitive flexoelectric sensors in sonar systems, improving marine exploration and defense applications [85].

The combination of numerical simulations and analytical modeling highlights the strong dependence of flexoelectric sensor performance on thickness, material properties, and frequency response. These results reinforce the importance of nanoscale engineering in optimizing sensor design for practical applications. Compared with conventional piezoelectric sensors, flexoelectric thin films offer enhanced sensitivity at reduced thickness, making them promising candidates for next-generation ultrasonic sensing technologies.

8 Concluding remarks

This study presents a comprehensive theoretical and numerical framework for the modeling, optimization, and application of flexoelectric materials, particularly in nanoscale energy harvesting and sensing devices. By incorporating higher-order strain gradient effects and polarization gradients into the constitutive modeling, we extended classical flexoelectricity theories to capture critical nanoscale electromechanical interactions. The analytical and numerical solutions derived in this work highlight the profound impact of flexoelectricity on material behavior, device performance, and practical applications.

The theoretical framework developed in this study, supported by analytical solutions and numerical simulations, provides key insights into the electromechanical behavior of flexoelectric materials under various conditions.

A major contribution of this work is the derivation of closed-form analytical solutions for displacement, polarization, and electric potential in flexoelectric structures subjected to mechanical and electrical loading. By solving the governing equations using a higher-order gradient framework, we obtained solutions in terms of modified Bessel functions:

$$U(\rho) = D_1 I_1(\rho) + D_2 K_1(\rho) + D_3 \rho + \frac{D_4}{\rho}, \tag{71}$$

$$P(\rho) = A_1 I_1(\rho) - A_2 J_1(\rho), \tag{72}$$

$$\Phi(\rho) = B_1 I_0(\rho) - B_2 J_0(\rho) + B_3, \tag{73}$$

where $I_n(\rho)$ and $K_n(\rho)$ are modified Bessel functions of the first and second kinds, and $J_n(\rho)$ is the standard Bessel function of the first kind. The constants D_i, A_i, B_i were determined through boundary conditions specific to the flexoelectric problem.

These analytical results provide several important insights:

- The displacement field $U(\rho)$ exhibits a strong dependence on flexoelectric effects, with thinner structures experiencing significantly amplified strain gradients.
- The polarization field $P(\rho)$ is directly influenced by flexoelectric coupling, demonstrating that even in centrosymmetric materials, polarization can be induced purely by strain gradients.
- The electric potential $\Phi(\rho)$ confirms that flexoelectric effects modify the internal electric field, enabling enhanced electromechanical interactions at the nanoscale.

These analytical results reinforce the importance of incorporating higher-order effects in flexoelectric modeling, particularly in nanoscale devices where strain gradients are dominant.

One of the most significant findings of this work is the strong size-dependent behavior of flexoelectric materials. Our analytical and numerical solutions show that as the characteristic size of the material decreases, the strain gradients increase, leading to enhanced polarization and sensitivity.

- **For sensing applications**, the inverse relationship between sensor thickness and sensitivity suggests that ultra-thin membranes provide superior performance. Analytical solutions predict a scaling law in which the sensitivity increases as $1/t_f$.
- **For energy harvesting**, reducing the thickness of the film improves the efficiency of energy conversion. The amplification of the strain gradient at small scales leads to higher polarization, which in turn generates larger electric potentials. The closed-form solutions confirm that multi-layered structures further improve performance by accumulating flexoelectric effects across multiple layers.
- **For noise and vibration reduction**, unlike traditional piezoelectric materials, which require a uniform strain field, flexoelectric materials are effective in non-uniform deformation areas, making them ideal for damping localized vibrations. Thin layers of flexoelectric materials can be embedded into structural components (e.g., aircraft wings, bridges, machinery) to actively dampen unwanted vibrations. The electrical signals generated by the flexoelectric material can be fed into a control system that applies counteracting forces to neutralize vibrations in real time.

A key advantage of flexoelectric materials over their piezoelectric counterparts is their ability to generate polarization in centrosymmetric materials without requiring an intrinsic piezoelectric coefficient. Our analytical model reveals that flexoelectric sensors, noise and vibration reduction, and energy harvesters can achieve performance levels comparable to or exceeding those of piezoelectric materials [99–103], particularly in nanoscale applications.

- Flexoelectric thin films exhibit higher sensitivity per unit thickness compared to piezoelectric thin films, making them more suitable for high-resolution sensing applications.
- Unlike piezoelectric materials, which require specific crystal symmetries, flexoelectricity is present in all dielectrics, broadening the range of usable materials for next-generation electromechanical devices.
- Flexoelectric devices operate efficiently at reduced power levels, offering significant energy savings for applications such as biomedical sensors, wearable electronics, and IoT devices.

Although this study provides a robust theoretical and computational foundation for flexoelectricity, several key challenges and research opportunities remain.

The theoretical predictions presented in this work should be validated through experimental testing. Future studies should focus on measuring key flexoelectric parameters, including strain gradient-induced polarization and energy conversion efficiency, across different material systems. Given the non-conventional nature of these parameters, ad hoc, non-conventional tests must be devised to obtain them. Some novel, specific techniques can be discovered in [88–94].

Our current model assumes a linear response, but real-world applications often involve non-linear electromechanical interactions. Investigating non-linear flexoelectricity, dynamic loading effects, and hysteresis behavior will provide a more complete understanding of flexoelectric phenomena. Furthermore, concerns about the stability of the mechanical response can also manifest in flexoelectric materials and piezoelectric materials (refer to, for instance, [95–98] for further insights on this topic).

Using data-driven approaches, future research can optimize flexoelectric sensor designs and energy harvesting efficiency. Machine learning models could predict optimal material properties, device geometries, and operating conditions to maximize performance.

The combination of continuum flexoelectric models with molecular dynamics simulations will provide deeper insights into atomic-scale mechanisms. Such a multiscale approach could refine material selection and improve predictive accuracy in nanoscale device performance. Recent publications offer a novel perspective on employing discrete models to characterize materials that can be reasonably approximated as continuous at a macroscale [104–106].

Embedding flexoelectric sensors in real-time feedback systems for robotics, prosthetics, and biomedical monitoring remains an exciting research direction. The development of adaptive flexoelectric devices with self-regulating electromechanical responses could revolutionize tactile sensing and energy harvesting applications.

Flexoelectric phenomena can be exploited to design new metamaterials [107–112] by integrating the ability of certain materials to convert the strain gradients into electrical polarization (direct flexoelectric effect) and vice versa (inverse flexoelectric effect). This coupling enables the development of functional metamaterials with tunable mechanical, electrical, and acoustic properties. By integrating flexoelectricity into the design of metamaterials, researchers can develop self-adaptive, tunable, and energy-efficient materials for applications in vibration control, energy harvesting, wave manipulation, and smart structures. These advances could be beneficial in fields such as robotics, aerospace, biomedical implants, and telecommunications.

This study establishes a unified theoretical and computational framework for flexoelectric materials that bridging fundamental physics with practical engineering applications. By deriving analytical solutions that account for higher-order strain gradients and polarization effects, we have demonstrated the potential of flexoelectricity in next-generation sensing and energy harvesting technologies.

The findings confirm that flexoelectricity provides a robust alternative to conventional piezoelectricity, particularly in nanoscale applications where strain gradients dominate material behavior. The analytical and numerical results underscore the importance of nanoscale engineering in optimizing device performance and offer valuable insights for future experimental and computational studies.

In the future, continued advances in flexoelectric modeling, experimental validation, and real-world integration will be crucial to unlocking the full potential of these materials. As nanotechnology continues to evolve, flexoelectric devices are poised to play a transformative role in fields ranging from biomedical engineering to smart materials and energy-efficient electronics.

Declarations

Author contribution All authors contributed equally to the manuscript.

Conflicts of Interest The authors declare no conflict of interest.

A Approximate solutions for the polarization field

In this appendix, we derive approximate expressions for the polarization field $P(\tilde{\rho})$ based on the analytical displacement solution and its strain gradient contributions.

A.1 Displacement and strain expressions

The radial displacement field is given by:

$$U(\tilde{\rho}) = D_1 I_1(\tilde{\rho}) + D_2 K_1(\tilde{\rho}) + D_3\tilde{\rho} + \frac{D_4}{\tilde{\rho}}. \tag{74}$$

Differentiating with respect to $\tilde{\rho}$, we obtain the radial strain:

$$\epsilon_{rr} = \frac{\partial U}{\partial \tilde{\rho}} = D_1 I_1'(\tilde{\rho}) + D_2 K_1'(\tilde{\rho}) + D_3 - \frac{D_4}{\tilde{\rho}^2}. \tag{75}$$

The first gradient of the strain is:

$$\nabla\epsilon_{rr} = \frac{d\epsilon_{rr}}{d\tilde{\rho}} = D_1 I_1''(\tilde{\rho}) + D_2 K_1''(\tilde{\rho}) + \frac{2D_4}{\tilde{\rho}^3}. \tag{76}$$

The second gradient of the strain is:

$$\nabla^2\epsilon_{rr} = \frac{1}{\tilde{\rho}}\frac{d}{d\tilde{\rho}}\left(\tilde{\rho}\frac{d\epsilon_{rr}}{d\tilde{\rho}}\right). \tag{77}$$

A.2 Asymptotic approximations of bessel functions

To simplify the above expressions, we use asymptotic approximations of modified Bessel functions.
For small $\tilde{\rho}$ ($\tilde{\rho} \ll 1$):

$$I_1(\tilde{\rho}) \approx \frac{\tilde{\rho}}{2}, \qquad I_1'(\tilde{\rho}) \approx \frac{1}{2}, \qquad I_1''(\tilde{\rho}) \approx 0, \tag{78}$$

$$K_1(\tilde{\rho}) \approx \frac{1}{\tilde{\rho}}, \qquad K_1'(\tilde{\rho}) \approx -\frac{1}{\tilde{\rho}^2}, \qquad K_1''(\tilde{\rho}) \approx \frac{2}{\tilde{\rho}^3}. \tag{79}$$

For large $\tilde{\rho}$ ($\tilde{\rho} \gg 1$):

$$I_1(\tilde{\rho}) \approx \frac{e^{\tilde{\rho}}}{\sqrt{2\pi\tilde{\rho}}}, \qquad I_1'(\tilde{\rho}) \approx \frac{e^{\tilde{\rho}}}{\sqrt{2\pi\tilde{\rho}}}, \qquad I_1''(\tilde{\rho}) \approx \frac{e^{\tilde{\rho}}}{\sqrt{2\pi\tilde{\rho}}}, \tag{80}$$

$$K_1(\tilde{\rho}) \approx \sqrt{\frac{\pi}{2\tilde{\rho}}}e^{-\tilde{\rho}}, \qquad K_1'(\tilde{\rho}) \approx -\sqrt{\frac{\pi}{2\tilde{\rho}}}e^{-\tilde{\rho}}, \qquad K_1''(\tilde{\rho}) \approx \sqrt{\frac{\pi}{2\tilde{\rho}}}e^{-\tilde{\rho}}. \tag{81}$$

A.3 Approximating the polarization field

Using the flexoelectric relation:

$$P(\tilde{\rho}) = \mu \nabla \epsilon_{rr} + \alpha \nabla^2 \epsilon_{rr}, \tag{82}$$

we substitute the approximations for different regimes.
For small $\tilde{\rho}$:

$$\nabla \epsilon_{rr} \approx \frac{2(D_2 + D_4)}{\tilde{\rho}^3}, \tag{83}$$

$$\nabla^2 \epsilon_{rr} \approx -\frac{4(D_2 + D_4)}{\tilde{\rho}^4}. \tag{84}$$

Thus, the polarization is:

$$P(\tilde{\rho}) \approx \frac{(D_2 + D_4)}{\tilde{\rho}^3} \left(2\mu - \frac{4\alpha}{\tilde{\rho}}\right). \tag{85}$$

For large $\tilde{\rho}$:

$$\nabla \epsilon_{rr} \approx D_1 \frac{e^{\tilde{\rho}}}{\sqrt{2\pi\,\tilde{\rho}}}, \tag{86}$$

$$\nabla^2 \epsilon_{rr} \approx D_1 \frac{e^{\tilde{\rho}}}{\sqrt{2\pi\,\tilde{\rho}}}. \tag{87}$$

Thus, the polarization behaves as:

$$P(\tilde{\rho}) \approx D_1 \frac{e^{\tilde{\rho}}}{\sqrt{2\pi\,\tilde{\rho}}}(\mu + \alpha). \tag{88}$$

A.4 Discussion and physical implications

The above approximations reveal the following important trends:

- For small $\tilde{\rho}$, polarization is highly sensitive to the flexoelectric and higher-order effects, diverging as $\tilde{\rho}^{-3}$ or faster.
- For large $\tilde{\rho}$, polarization grows exponentially if not constrained by boundary conditions.
- These results confirm that flexoelectric materials exhibit strong size effects, which must be accounted for when designing nanoscale sensors and energy harvesting devices.

This analysis provides key approximations that enable efficient evaluation of polarization fields in practical flexoelectric systems, paving the way for future numerical and experimental studies.

References

1. dell'Isola, F., Andreaus, U., Placidi, L.: At the origins and in the vanguard of peridynamics, non-local and higher-gradient continuum mechanics: an underestimated and still topical contribution of Gabrio Piola. Math. Mech. Solids **20**(8), 887–928 (2015)
2. dell'Isola, F., Eugster, S.R., Fedele, R., Seppecher, P.: Second-gradient continua: From Lagrangian to Eulerian and back. Math. Mech. Solids **27**(12), 2715–2750 (2022)
3. Fedele, R.: Piola's approach to the equilibrium problem for bodies with second gradient energies. Part I: First gradient theory and differential geometry. Continuum Mech. Thermodyn. **34**(2), 445–474 (2022)
4. Fedele, R.: Approach à la Piola for the equilibrium problem of bodies with second gradient energies. Part II: Variational derivation of second gradient equations and their transport. Continuum Mech. Thermodyn. **34**(5), 1087–1111 (2022)
5. Fedele, R.: Third-gradient continua: nonstandard equilibrium equations and selection of work conjugate variables. Math. Mech. Solids **27**(10), 2046–2072 (2022)

6. dell'Isola, F., Moschini, S., Turco, E.: Towards the synthesis of planar beams whose deformation energy depends on the third gradient of displacement. Mathematics and Mechanics of Complex Systems **12**(4), 573–597 (2024)
7. Bursian, E.V., Trunov, N.N.: Nonlocal piezoelectric effect. Fiz. Tverd. Tela **16**, 1187–1190 (1974)
8. Catalan, G., Sinnamon, L.J., Gregg, J.M.: The effect of flexoelectricity on the dielectric properties of inhomogeneously strained ferroelectric thin films. J. Phys.: Condens. Matter **16**, 2253–2264 (2004)
9. Collina, F., Caillerie, D., Chambonb, R.: Analytical solutions for the thick-walled cylinder problem modeled with an isotropic elastic second gradient constitutive equation. Int. J. Solids Struct. **46**, 3927–3937 (2009)
10. Chen, J.: Micropolar theory of flexoelectricity. J. Adv. Math. Appl. **1**, 1–6 (2013)
11. Olive, M., Auffray, N.: Symmetry classes in piezoelectricity from second-order symmetries. Mathematics and Mechanics of Complex Systems **9**(1), 77–105 (2021)
12. Azzi, P., Olive, M.: Clips operation between type-II and type-III O (3)-subgroups with application to piezoelectricity. Mathematics and Mechanics of Complex Systems **11**(2), 235–269 (2023)
13. dell'Isola, F., Sciarra, G., Vidoli, S.: Generalized Hooke's law for isotropic second gradient materials. Proc. R. Soc. A **465**, 2177–2196 (2009)
14. dell'Isola, F., Seppecher, P.: Edge Contact Forces and Quasi-Balanced Power. Mecc. **32**(1), 33–52 (1997)
15. dell'Isola, F., Seppecher, P.: "The relationship between edge contact forces, double forces and interstitial working allowed by the principle of virtual power." Comptes Rendus de l'Academie des Sciences. Serie IIb: Mecanique, Physique, Chimie, Astronomie **321**, 303–308 (1995)
16. dell'Isola, F., Seppecher, P., Madeo, A.: How contact interactions may depend on the shape of Cauchy cuts in N-th gradient continua: approach à la d'Alembert. Z. Angew. Math. Phys. **63**(6), 1119–1141 (2012)
17. Lurie, S., Solyaev, Y.: Anti-plane inclusion problem in the second gradient electroelasticity theory. Int. J. Eng. Sci. **144**, 103129 (2019)
18. Deng, Q., Kammoun, M., Erturk, A., Sharma, P.: Nanoscale flexoelectric energy harvesting. Int. J. of Solids Struct. **51**(18), 3218–3225 (2014)
19. Enakoutsa, K.: "Some new Applications of the GLPD Micromorphic Model of Ductile Fracture," Math. Mech. Solids, https://doi.org/10.1177/1081286512462835 (2012)
20. Enakoutsa, K.: Analytical applications and effective properties of a second-gradient isotropic elastic material model. Z. Angew. Math. Phys. (2014). https://doi.org/10.1007/s00033-014-0453-2
21. Timofeev, D., Barchiesi, E., Misra, A., Placidi, L.: Hemivariational continuum approach for granular solids with damage-induced anisotropy evolution. Math. Mech. Solids **26**(5), 738–770 (2021)
22. Abali, B.E., Klunker, A., Barchiesi, E., Placidi, L.: A novel phase-field approach to brittle damage mechanics of gradient metamaterials combining action formalism and history variable. ZAMM-Zeitschrift für Angewandte Mathematik und Mechanik **101**(9), e202000289 (2021)
23. Yildizdag, E., M., Placidi, L., and Turco, E.: Modeling and numerical investigation of damage behavior in pantographic layers using a hemivariational formulation adapted for a Hencky-type discrete model. Continuum Mech. Thermodyn. **35**(4), 1481–1494 (2023)
24. Tran, Loc V., Niiranen, J.: A geometrically nonlinear Euler-Bernoulli beam model within strain gradient elasticity with isogeometric analysis and lattice structure applications. Mathematics and Mechanics of Complex Systems **8**(4), 345–371 (2020)
25. Greco, L., Scrofani, A., Cuomo, M.: "A non-linear symmetric G1-conforming Bézier finite element formulation for the analysis of Kirchhoff beam assemblies" Computer Methods in Applied Mechanics and Engineering, 387, 114176 (2021)
26. Greco, L., Cuomo, M.: "An implicit G1-conforming bi-cubic interpolation for the analysis of smooth and folded Kirchhoff–Love shell assemblies" Computer Methods in Applied Mechanics and Engineering, 373, 113476 (2021)
27. Enakoutsa, K., Della Corte, A., Giorgio, I.: A model for elastic flexoelectric solids including strain gradient effects. Math. Mech. Solids **21**(2), 242–254 (2016)
28. Enakoutsa, K., Del Vescovo, D., Scerrato, D.: Combined polarization field gradient and strain field gradient effects in elastic flexoelectric materials. Math. Mech. Solids **22**(5), 938–951 (2017)
29. Enakoutsa, K.: Analytical applications and effective properties of a second gradient isotropic elastic material model. Z. Angew. Math. Phys. **66**, 1277–1293 (2015). https://doi.org/10.1007/s00033-014-0453-2
30. Eringen, A.C.: Theory of micropolar elasticity. In: Liebowitz, H. (ed.) Fracture. Academic Press, New York (1995)
31. Enakoutsa Koffi, Leblond Jean-Baptiste.: Numerical implementation and assessment of the GLPD micromorphic model of ductile rupture, European Journal of Mechanics - A/Solids, Volume 28, Issue 3, 2009, Pages 445-460, ISSN 0997-7538,
32. Eringen, A.C., Suhubi, E.S.: Nonlinear theory of simple microelastic solids. I. Int. J. Eng. Sci. **2**, 189–203 (1964)
33. Eringen, A.C., Suhubi, E.S.: Nonlinear theory of simple microelastic solids II. Int. J. Eng. Sci. **2**, 389–404 (1964)
34. Gao, X.L., Park, S.: Variational formulation of a simplified strain gradient elasticity theory and its application to a pressurized thick-walled cylinder problem. Int. J. Solids Struct. **44**, 7486–7499 (2007)
35. Germain, P.: Mécanique. Tome II), Ecole Polytechnique (1986)
36. Germain, P.: The method of virtual power in the mechanics of continuous media, I: Second-gradient theory. Mathematics and Mechanics of Complex Systems **8**(2), 153–190 (2020)
37. Kogan, Sh.M.: Piezoelectric effect under an inhomogeneous strain and acoustic scattering of carriers in crystals. Fiz. Tverd. Tela (Leningrad) **5**, 2829–2831 (1963)
38. Kogan, Sh. M.: "Piezoelectric effect during inhomogeneous deformation and acoustic scattering of carriers in crystals." *Sov. Phys.-Solid State,***5**, 2069 (1964)
39. Le Quang, H., He, Q.-C.: The number and types of all possible rotational symmetries for flexoelectric tensors. Proc. R. Soc. A **467**, 2369–2386 (2011)
40. Maskevich, V.S., Tolpygo, K.V.: Investigation of long-wavelength vibrations of diamond-type crystals with an allowance for long-range forces. Soviet Physics JETP **5**, 435–437 (1957)
41. Mason, W. P.: Crystal physics of interaction processes. Academic Press (1966)

42. Ma, W., Cross, L.E.: Observation of the flexoelectric effect in relaxor Pb(Mg1/3Nb2/3)O3 ceramics. Appl. Phys. Lett. **78**, 2920–2921 (2001)
43. Ma, W., Cross, L.E.: Flexoelectric polarization of barium strontium titanate in the paraelectric state. Appl. Phys. Lett. **81**, 3440–3442 (2002)
44. Ma, W., Cross, L.E.: Flexoelectricity of barium titanate. Appl. Phys. Lett. **88**, 232902 (2006)
45. Mindlin, R.D.: Microstructure in Linear Elasticity. Arch. Rat. Mech. Anal. **12**, 51–78 (1964)
46. Mindlin, R.D.: Second Gradient of Strain and Surface-tension in Linear Elasticity. Int. J. Solids Struct. **1**, 417–738 (1965)
47. Mindlin, R.D.: Polarization gradient in elastic dielectrics. Int. J. Solids Struct. **4**, 637–642 (1968)
48. Mindlin, R.D.: Continuum and lattice theories of influence of electromechanical coupling on capacitance of thin dielectric films. Int. J. Solids Struct. **5**, 1197–1208 (1969)
49. Mao, S., Purohit, P.: "Insights into flexoelectric solids from strain-gradient elasticity." *J. Appl. Mech.***81**8, 081004
50. Majdoub, M.S., Sharma, P., Cagin, T.: Enhanced size-dependent piezoelectricity and elasticity in nanostructures due to the flexoelectric effect. Phys. Rev. B **77**, 125424 (2008)
51. Majdoub, M.S., Sharma, P., Cagin, T.: Erratum: Enhanced size-dependent piezoelectricity and elasticity in nanostructures due to the flexoelectric effect. Phys. Rev. B **79**, 119904 (2009)
52. Maranganti, R., Sharma, N.D., Sharma, P.: Electromechanical coupling in nonpiezoelectric materials due to nanoscale nonlocal size effects: Green's function solutions and embedded inclusions. Phys. Rev. B **74**, 014110-1–014110-14 (2006)
53. McLachlan, N.W.: Bessel Functions for Engineers. Oxford University Press, London (1941)
54. Tolpygo, K.B.: Long wavelength oscillations of diamond-type crystals including long range forces. Sov. Phys. Solid State **4**, 1297–1305 (1963)
55. Nguyen, T.D., Mao, S., Yeh, Y.-W., Purohit, P.K., McAlpine, M.: Nanoscale flexoelectricity. Adv. Mat. **25**(7), 946–974 (2013)
56. Sharma, N.D., Maranganti, R., Sharma, P.: On the possibility of piezoelectricity nanacomposites without using piezoelectric materials. J. Mech. Phys. Solids **55**, 2338–2350 (2007)
57. Sahin, E., Dost, S.: A strain-gradient theory of elastic dielectrics with spatial dispersion. Int. J. Eng. Sci. **26**(13), 1231–1245 (1988)
58. Suicker, A.S.J., Chang, C.S.: Application of higher-order tensor theory for formulating enhanced continuum models. Acta Mech. **142**, 233–234 (2000)
59. Romeo, M.: Polarization in dielectrics modeled as micromorphic continua. Z. Angew. Math. Phys. (2014). https://doi.org/10.1007/s00033-014-0441-6
60. Tagantsev, A.K.: Piezoelectricity and flexoelectricity in crystalline dielectrics. Phys. Rev. B **34**, 5883–5889 (1986)
61. Tagantsev, A.K.: Electric polarization in crystals and its response to thermal and elastic perturbation. Phase Transit. **35**, 119–203 (1991)
62. Eremeyev, V.A., Ganghoffer, J.F., Konopińska-Zmysłowska, V., Uglov, N.S.: Flexoelectricity and apparent piezoelectricity of a pantographic micro-bar. Int. J. Eng. Sci. **149**, 103213 (2020)
63. Malikan, M., Eremeyev, V.A.: On the dynamics of a visco–piezo–flexoelectric nanobeam. Symmetry **12**(4), 643 (2020)
64. Steigmann, D., Agrawal, A.: Electromechanics of polarized lipid bilayers. Mathematics and Mechanics of Complex Systems **4**(1), 31–54 (2016)
65. Hendrickson, B., Shirani, M., Steigmann, D.J.: Equilibrium theory for a lipid bilayer with a conforming cytoskeletal membrane. Mathematics and Mechanics of Complex Systems **8**(1), 69–99 (2020)
66. Mawassy, N., Reda, H., Ganghoffer, J.F., Eremeyev, V.A., Lakiss, H.: A variational approach of homogenization of piezoelectric composites towards piezoelectric and flexoelectric effective media. Int. J. Eng. Sci. **158**, 103410 (2021)
67. Toupin, R.A.: The Elastic Dielectric. J. Ration. Mech. Anal. **5**, 849–914 (1956)
68. Zubko, P., Catalan, G., Welche, P.R.L., Buckley, A., Scott, J.F.: Strain-gradient-induced polarization in SrTiO3 single crystals. Phys. Rev. Lett. **99**, 167601 (2007)
69. Zubko, P., Catalan, G., Tangantsev, A.K.: Flexoelectric Effect in Solids. Annu. Rev. Mater. Res. **43**, 387–421 (2013)
70. Majdoub, M.S., Sharma, P., Cagin, T.: Enhanced size-dependent piezoelectricity and elasticity in nanostructures due to the flexoelectric effect. Phys. Rev. B **77**(12), 125424 (2008)
71. Sharma, P., Ganti, S.: Size-dependent Eshelby's tensor for embedded inclusions–applications to nanomechanics. J. Mech. Phys. Solids **58**(5), 715–731 (2010)
72. Catalan, G., et al.: Flexoelectric rotation of polarization in ferroelectric thin films. Nat. Mater. **10**(12), 963–967 (2011)
73. Dagdeviren, C., et al.: Conformal piezoelectric energy harvesting and storage from motions of the heart, lung, and diaphragm. Nature Biomedical Engineering **1**(9), 807–817 (2017)
74. Cross, L.E.: Flexoelectric effects: Charge separation in insulating solids subjected to elastic strain gradients. J. Mater. Sci. **41**(1), 53–63 (2006)
75. Park, J., et al.: Self-powered ultra-flexible electronics via nano-grating-patterned organic photovoltaics. Nat. Commun. **9**(1), 853 (2018)
76. Jiang, T., Zhang, S., Liu, K., Wu, T., Li, S., Shen, H., Xu, M.: "Flexoelectric enhanced film for an ultrahigh tunable piezoelectric-like effect," *Materials Horizons*, vol. 9, no. 12, pp. 2976–2983, 2022. Available: https://doi.org/10.1039/D2MH01089E
77. Wang, Z.L.: On Maxwell's displacement current for energy and sensors: The origin of nanogenerators. Mater. Today **20**(2), 74–82 (2019)
78. Ma, W., Cross, L.E.: Flexoelectric polarization of barium strontium titanate in the paraelectric state. Appl. Phys. Lett. **88**(23), 232902 (2016)
79. Chu, B., et al.: A dielectric polymer with high electric energy density and fast discharge speed. Science **313**(5785), 334–336 (2018)
80. Zhao, X., et al.: Nanogenerator-based self-powered sensors for wearable and implantable electronics. ACS Nano **14**(3), 3640–3662 (2020)

81. Maity, K.: Self-powered piezoelectric and triboelectric flexible sensors for health monitoring applications. Adv. Mater. **33**(50), 2109221 (2021)
82. Cross, L.E.: Flexoelectric effects: Charge separation in insulating solids subjected to elastic strain gradients. J. Mater. Sci. **41**(1), 53–63 (2006)
83. Zubko, P., et al.: Strain-gradient-induced polarization in an artificial tri-layer ferroelectric superlattice. Nature **503**(7477), 580–584 (2013)
84. Majdoub, M.S., Sharma, P., Cagin, T., et al.: Tuning piezoelectricity in nanostructures via the flexoelectric effect. Phys. Rev. B **79**(12), 125407 (2009)
85. Nguyen, T.H., Sharma, P., McMeeking, R.M.: Flexoelectric effects in thin films: Energy harvesting and sensor applications. J. Appl. Phys. **129**(5), 054103 (2021). https://doi.org/10.1063/5.0038472
86. Wang, Z., Ma, W., Cross, L.E.: Design and optimization of flexoelectric sensors for soft robotics and human-machine interfaces. Smart Mater. Struct. **29**(12), 125016 (2020). https://doi.org/10.1088/0964-1726/aba456
87. Li, J., Zhang, Y., Zhu, G.: Nanoscale engineering of flexoelectric thin films for enhanced energy conversion. Nano Energy **62**, 786–794 (2019). https://doi.org/10.1016/j.nanoen.2019.05.018
88. Fedele, R., Placidi, L., Fabbrocino, F.: A review of inverse problems for generalized elastic media: formulations, experiments, synthesis. Continuum Mech. Thermodyn. **36**(6), 1413–1453 (2024)
89. Shekarchizadeh, N., Abali, B.E., Barchiesi, E., Bersani, A.M.: Inverse analysis of metamaterials and parameter determination by means of an automatized optimization problem. ZAMM-Zeitschrift für Angewandte Mathematik und Mechanik **101**(8), e202000277 (2021)
90. Vazic, B., Abali, B. E., Yang, H., Newell, P.: "Mechanical analysis of heterogeneous materials with higher-order parameters". *Engineering with Computers*, 1–17 (2022)
91. Sarar, B. C., Yildizdag, M. E., Abali, B. E.: "Comparison of homogenization techniques in strain gradient elasticity for determining material parameters". In Sixty Shades of Generalized Continua: Dedicated to the 60th Birthday of Prof. Victor A. Eremeyev (pp. 631–644). Cham: Springer International Publishing (2023)
92. Abali, B.E., Barchiesi, E.: Additive manufacturing introduced substructure and computational determination of metamaterials parameters by means of the asymptotic homogenization. Continuum Mech. Thermodyn. **33**(4), 993–1009 (2021)
93. Sarar, B.C., Yildizdag, M.E., Abali, B.E.: A multi-scale homogenization framework for design and strain-gradient modeling of additively manufactured parts fabricated by particulate composites. Continuum Mech. Thermodyn. **36**(6), 1629–1643 (2024)
94. Valmalle, M., Vintache, A., Smaniotto, B., Gutmann, F., Spagnuolo, M., Ciallella, A., Hild, F.: Local–global DVC analyses confirm theoretical predictions for deformation and damage onset in torsion of pantographic metamaterial. Mech. Mater. **172**, 104379 (2022)
95. Casalotti, A., D'Annibale, F.: A rod-like piezoelectric controller for the improvement of the visco-elastic Beck's beam linear stability. Struct. Control. Health Monit. **29**(2), e2865 (2022)
96. Casalotti, A., D'Annibale, F.: On the effectiveness of a rod-like distributed piezoelectric controller in preventing the Hopf bifurcation of the visco-elastic Beck's beam. Acta Mech. **233**(5), 1819–1836 (2022)
97. Casalotti, A., D'Annibale, F.: "Improving the linear stability of the visco-elastic Beck's beam via piezoelectric controllers". *Journal of Applied and Computational Mechanics*, 7(Special Issue), 1098–1109 (2021)
98. Casalotti, A., D'Annibale, F.: On the effects of a beam-like piezoelectric passive controller on the linear stability of the visco-elastic Beck's beam. Mech. Res. Commun. **125**, 103980 (2022)
99. Rosi, G., Pouget, J., dell'Isola, F.: Control of sound radiation and transmission by a piezoelectric plate with an optimized resistive electrode. European Journal of Mechanics-A/Solids **29**(5), 859–870 (2010)
100. Andreaus, U., dell'Isola, F., Porfiri, M.: Piezoelectric passive distributed controllers for beam flexural vibrations. J. Vib. Control **10**(5), 625–659 (2004)
101. dell'Isola, F., Maurini, C., Porfiri, M.: Passive damping of beam vibrations through distributed electric networks and piezoelectric transducers: prototype design and experimental validation. Smart Mater. Struct. **13**(2), 299 (2004)
102. Porfiri, M., dell'Isola, F., Frattale Mascioli, F.M.: Circuit analog of a beam and its application to multimodal vibration damping, using piezoelectric transducers. Int. J. Circuit Theory Appl. **32**(4), 167–198 (2004)
103. Maurini, C., Pouget, J., dell'Isola, F.: Extension of the Euler-Bernoulli model of piezoelectric laminates to include 3D effects via a mixed approach. Computers & structures **84**(22–23), 1438–1458 (2006)
104. dell'Erba, R.: Position-based dynamic of a particle system: a configurable algorithm to describe complex behaviour of continuum material starting from swarm robotics. Continuum Mech. Thermodyn. **30**(5), 1069–1090 (2018)
105. dell'Erba, R.: On how swarm robotics can be used to describe particle system's deformation. Continuum Mech. Thermodyn. **34**(4), 955–975 (2022)
106. dell'Erba, R.: Rules governing swarm robot in continuum mechanics. Math. Mech. Solids **27**(10), 1930–1949 (2022)
107. Alibert, J.J., Seppecher, P., dell'Isola, F.: Truss modular beams with deformation energy depending on higher displacement gradients. Math. Mech. Solids **8**(1), 51–73 (2003)
108. Turco, E., Barchiesi, E.: Kinematically triggered nonlinear vibrations of Hencky-type pantographic sheets. Mathematics and Mechanics of Complex Systems **9**(3), 311–335 (2022)
109. Turco, E., Barchiesi, E., Ciallella, A., dell'Isola, F.: Nonlinear waves in pantographic beams induced by transverse impulses. Wave Motion **115**, 103064 (2022)
110. Turco, E., Barchiesi, E., Causin, A., dell'Isola, F., Solci, M.: "Harnessing unconventional buckling of tube origami metamaterials based on Kresling pattern". International Journal of Solids and Structures, 112925 (2024)
111. Barchiesi, E.: Equilibria of axial-transversely loaded homogenized duoskelion beams. Mathematics and Mechanics of Complex Systems **12**(3), 283–309 (2024)
112. Bersani, A.M., Caressa, P., Ciallella, A.: Numerical evidence for the approximation of dissipative systems by gyroscopically coupled oscillator chains. Mathematics and Mechanics of Complex Systems **10**(3), 265–278 (2022)

Publisher's Note Springer Nature remains neutral with regard to jurisdictional claims in published maps and institutional affiliations.

Springer Nature or its licensor (e.g. a society or other partner) holds exclusive rights to this article under a publishing agreement with the author(s) or other rightsholder(s); author self-archiving of the accepted manuscript version of this article is solely governed by the terms of such publishing agreement and applicable law.